Chapter 7

Modeling Impulsive Phase Solar Flares: a Combined Hydrodynamic and Fokker-Planck Approach

7.1 Introduction

Particle acceleration & transport and the dynamical response of the atmosphere are two of various important processes of energization and dynamics involved in solar flares. As mentioned earlier in Chapter 1, these two processes are in fact coupled and must be studied together in a self-consistent way. Due to the forbidding complexity of the subject, however, people tend to decouple the processes and study one at a time while assuming some simple forms for the others. The past efforts, according to their focus, can be divided into two categories: particle acceleration and/or transport and atmospheric response.

For the former, one of the main streams of study solves the Fokker-Planck equation and and keeps track of the particle distribution function (while there have been researchers who took the approach of Monte Carlo simulation). For example, by assuming a static atmosphere model, particle transport (including Coulomb collision and magnetic mirroring) was studied by Leach & Petrosian (1981) and was extended to the relativistic regime (including synchrotron loss and pitch-angle scattering) by McTiernan & Petrosian (1990). Other similar studies were performed by MacKinnon & Craig (1991), McClements (1992), Syniavskii & Zharkova (1994), Zharkova et al. (1995). Particle acceleration by turbulence, for instance, was investigated by Hamilton & Petrosian (1992), Miller et al. (1996), Park et al. (1997), Petrosian & Liu (2004) in more recent years.

For the atmospheric response, although the solar atmosphere is magnetized and thus a full magnetohydrodynamic (MHD) description is desired, a majority of efforts were put into numerical hydrodynamic (HD) simulations assuming a fixed magnetic configuration. Because in a low β (magnetic field dominated) environment as in the solar corona, the plasma cannot move across the magnetic field line readily, it is reasonable to assume the material flow follows the magnetic field, which justifies 1D (distance along the magnetic field line) HD models. These models usually assume a simple spectrum of the accelerated particles which are injected at the apex of the loop and the energy deposited by the particles

at different distances along the loop is calculated in a simplified way. This energy deposition, which drives fluid dynamics, is the input to the HD code. Such studies include Nagai & Emslie (1984), Fisher et al. (1985a,b,c), Mariska et al. (1989), Gan & Fang (1990), and recent works by Abbett & Hawley (1999), and Allred et al. (2005).

From a theoretical point of view, a combined treatment of particle acceleration and transport and the atmospheric response has become progressively desired and doable, based on advances in both directions over two decades and particularly in recent years. Miller has made progress (Miller & Mariska, 2005) in coupling his stochastic particle acceleration code (Miller et al., 1996) with the Naval Research Laboratory (NRL) Solar Flux Tube Model hydrodynamic code (Mariska, Li, & Emslie 1989, hereafter MEL89). Winter & Martens (2006) combine their Monte Carlo simulation of test particle dynamics and a similar HD code. They inject a power-law electron beam at the apex of the loop and tracked the particle transport and the atmospheric response processes.

From an observational point of view, new observations, particularly X-ray images and spectra obtained by the recent *RHESSI* satellite and the previous *Yohkoh* satellite, have posed new challenges and questions to theories. For example, we (Liu, W. et al., 2006) reported an event of chromospheric evaporation imaged by *RHESSI* for the first time. As shown in Chapter 6, during this event, HXR sources at intermediate energies (12-15 keV) were observed to appear at the leg of the flaring loop, in contrast to the commonly observed LT and FP sources at low and high energies, respectively. Such sources shifted from the FPs to the LT as time progressed, and exhibited very high speeds ($\sim 10^3$ km s^{-1}) during several short time intervals. Surprisingly, our Neupert (1968) effect test revealed that the electron energy power, a more physically relevant quantity, did not yield a better correlation with the *GOES* SXR flux derivative than the more conventional HXR flux. To fully understand these observations and address the apparent discrepancies, again, requires a coupled treatment of the particle acceleration and transport and the atmospheric response processes.

An accurate treatment of this problem requires a detailed evaluation of the heating rate by nonthermal electrons, which is a key input to flare HD simulations. Previous works in this regard suffer from two major shortcomings. (1) The first is that the calculation of the energy deposition is based on approximate analytical solutions (e.g., Brown, 1973a; Emslie, 1978). This can be remedied by a combined particle and HD simulation, with the inclusion of a full Fokker-Planck treatment of the electron transport. (2) The other drawback is the simple, non-realistic, form of the injected electron spectrum used, which was usually assumed to be some form of power-law distribution that makes the solution analytically tractable. Fisher et al. (1985c), for example, assumed a power-law spectrum with an index of $\delta = 4$ and a sharp low-energy cutoff at $E_1 = 20$ keV (i.e., no electrons below E_1). MEL89 introduced a "soft" cutoff, below which the spectrum is a power-law with a positive index of 2. Recently, Allred et al. (2005)[1] used a comparably more realistic broken power-law electron spectrum derived from *RHESSI* observations (Holman et al., 2003). As we will show later, the heating rate is sensitive to the electron spectrum and thus use of inaccurate spectrum would make the HD result deviate from reality significantly. On the basis of the SA model, Petrosian & Liu (2004) have provided a more realistic electron spectrum that has a continuous form from a background thermal distribution at low energies to a nonthermal

[1]They also improved the heating rate calculation by adopting the technique of Hawley & Fisher (1994) to include the variation of hydrogen ionization state and by calculating radiative transfer and XEUV heating.

distribution at high energies. We use such an spectrum in the work described below. We will see that the low-energy electrons play an important role in heating (via collision and conduction) and in affecting the subsequent hydrodynamical process.

In this chapter, we present a review of the Fokker-Planck modeling and show it can be combined with a HD simulation of the atmospheric response during the impulsive phase (§7.2). The former component uses the unified code of particle acceleration, transport, and bremsstrahlung radiation (Petrosian et al., 2001). The latter uses the NRL Solar Flux Tube Model code (MEL89). We obtained the spatial distribution and temporal evolution of the resulting HXRs and SXRs, and check them against available *RHESSI* observations (e.g., Liu, W. et al., 2006; Sui et al. 2006). Results from some model calculations are presented in §7.3. We summarize the major findings of this chapter and draw conclusions in §7.4.

7.2 Simulation Models

7.2.1 Stochastic Acceleration Model

Here we briefly summarize the acceleration model used in this study, which was adopted from Petrosian & Liu (2004, hereafter PL04). We focus on acceleration by waves that propagate parallel to the background magnetic field.

The Fokker-Planck Equation

Let us rewrite the Fokker-Planck (F-P) equation that governs electron acceleration (eq. [1.1])

$$\frac{\partial f_{\rm ac}}{\partial t} = \frac{\partial}{\partial E}\left[D(E)\frac{\partial f_{\rm ac}}{\partial E}\right] + \frac{\partial}{\partial E}\{[A(E) - \dot{E}_L]f_{\rm ac}\} - \frac{f_{\rm ac}}{T_{\rm esc}(E)} + Q(E)\,. \tag{7.1}$$

where $f_{\rm ac} \equiv f_{\rm ac}(t, E)$ is the electron distribution function (in units of electrons $\rm cm^{-3}\,keV^{-1}$, integrated over all pitch angles; the subscript "ac" denotes acceleration region, cf. the $f(E, s, \mu)$ in the transport code), $E = \gamma - 1$ (γ being the Lorentz factor) is the electron kinetic energy in units of $m_e c^2$ (m_e is the electron mass), $D(E)$ and $A(E)$ are the energy diffusion and systematic acceleration coefficients, $T_{\rm esc}$ is the particle escape time, $Q(E)$ is the total injection flux of particles into the acceleration region that acts as source term in the equation.

$$\dot{E}_L = \dot{E}_{\rm Coul} + \dot{E}_{\rm synch} \tag{7.2}$$

is the absolute value of the net systematic energy loss rate, which is a combination of Coulomb loss (assuming a cold background plasma)

$$\dot{E}_{\rm Coul} = 4\pi r_0^2 \ln\Lambda c n_e/\beta\,, \tag{7.3}$$

and synchrotron loss

$$\dot{E}_{\rm synch} = 4 r_0^2 B^2 \beta^2 \gamma^2 / 9 m_e c\,, \tag{7.4}$$

where $\beta = v/c$, n_e is the electron number density, $r_0 = e^2/m_e c^2 = 2.8 \times 10^{-13}\,\rm cm$ is classical electron radius, $\ln\Lambda = 20$ (good for coronal conditions, Leach 1984) is the Coulomb logarithm, and B is the background magnetic field. Note equation (7.4) is valid only for

isotropic pitch-angle distribution, which is assumed to be the case in the acceleration region because of strong scattering of particles by turbulence.

In order to solve the F-P equation and keep tracking the evolution of the distribution function $f_{\rm ac}(t,E)$, one needs to know all the terms in the equation. Since the form of the energy loss rates are well known and the injection flux $Q(E)$ (say, thermal or Maxwellian distribution) is to be assumed by specific models, the central task left is to determine the diffusion coefficient $D(E)$, the direct acceleration rate $A(E)$, and the escape time $T_{\rm esc}$, which we describe as follows.

Dispersion Relation and Resonance Condition

In general, plasma waves can be described by their dispersion relations, and when particles are accelerated by turbulence, the wave-particle interaction is determined by the resonance condition.

We assume a fully ionized H and ^{4}He plasma with the relative abundance of electron/proton/α-particle = 1/0.84/0.08. The **dispersion relation** for parallel propagating waves in such a plasma is:

$$\frac{k^2}{\omega^2}=1-\frac{\alpha^2}{\omega}\left[\frac{1}{\omega-1}+\frac{(1-2Y_{\rm He})\delta}{\omega+\delta}+\frac{Y_{\rm He}\delta}{\omega+\delta/2}\right], \tag{7.5}$$

where ω *is the wave frequency in units of the nonrelativistic electron gyrofrequency* $\Omega_e=(eB_0)/(m_ec)$ (e is the electron charge and B_0 the large-scale magnetic field), k *is the wavenumber in units of* Ω_e/c, $Y_{\rm He}=0.08$ is the ^{4}He abundance, the *plasma parameter* α and the electron-to-proton mass ratio δ are given by

$$\alpha=\omega_{pe}/\Omega_e=3.2(n_e/10^{10}{\rm cm}^{-3})^{1/2}(B_0/100\,{\rm G})^{-1}\quad\text{and}\quad\delta=m_e/m_p\,, \tag{7.6}$$

where $\omega_{pi}=(4\pi n_e e^2/m_e)^{1/2}$ is the electron plasma frequency and m_p is the proton mass. From this dispersion relation, we have five distinct wave modes (branches): electromagnetic wave branch (EM), electron-cyclotron branch (EC), modified proton-cyclotron branch (PC'), ^{4}He-cyclotron branch (HeC), and a second electromagnetic wave branch (EM') (see PL04, Fig. 11, for details).

Via the **resonance wave-particle interaction**, energy can be transferred from particles to waves and vice versa (Dung & Petrosian, 1994). For a particle with a velocity βc and a pitch-angle cosine μ the resonance condition can be written as

$$\omega-k_{||}\beta\mu=\frac{n\omega_i}{\gamma}\,, \tag{7.7}$$

where n is the harmonic number of the gyrofrequency (not particle number density), $k_{||}$ is the parallel component of the wave vector, $\omega_i=q_im_e/em_i$ is the particle gyrofrequency in units of Ω_e. In our case of electron acceleration by parallel waves, $k_{||}=k$, $n=-1$, $\omega_e=-1$ (while $\omega_p=m_e/m_p=\delta$ for protons), and the resonance condition reduces to

$$\omega-k\beta\mu=\frac{1}{\gamma}\,. \tag{7.8}$$

It appears as a straight line in the k–ω plot, with the $v=\beta\mu$ being the slope and $1/\gamma$ being

the intercept. For an electron with a given velocity and pitch angle, in order to determine how it is accelerated by waves, one must first need to determine with which wave branch(es) (see PL04, Fig. 11) and at what frequency (or wave number) this straight line intersect. That is, one needs to find the roots k_j and their corresponding ω_j ($j = 1, ..., N$) of the combined nonlinear equations (7.5) and (7.8), which is done numerically in the SA code. Because of the complexity of the dispersion relation and the large dynamic range of the wavenumber, it is not a trivial task to accurately find the roots. For different particles, say, electrons and protons, their roots are located on different branches, and thus they are accelerated at different rates (see PL04, e.g., Fig. 12 for a comparison).

Turbulence Spectrum and Fokker-Planck Coefficients

To determine how much energy a particle can gain from its interaction with waves, one also needs to know the **energy spectrum of the turbulence**. Following PL04, we assume a turbulence spectrum of a broken power-law with three indexes q, $q_{\rm l}$ and $q_{\rm h}$ and two critical wavenumbers $k_{\rm min}$ and $k_{\rm max}$,

$$\mathcal{E}(k) = (q-1)\mathcal{E}_0/k_{\rm min} \begin{cases} (k/k_{\rm min})^{q_{\rm l}}, & \text{for } k < k_{\rm min}; \\ (k/k_{\rm min})^{-q}, & \text{for } k_{\rm min} < k < k_{\rm max}; \\ (k_{\rm max}/k_{\rm min})^{-q}(k/k_{\rm max})^{-q_{\rm h}}, & \text{for } k > k_{\rm max}, \end{cases} \tag{7.9}$$

where we choose $q_{\rm l} = 2 (> 0)$, $q = 1.7$ is the Kolmogorov value, and $q_{\rm h} = 4$ is a typical index for waves subject to strong damping (Vestuto et al., 2003). The cutoff at high wavenumber $k_{\rm max}$ is assumed to be caused by, say, thermal damping. Following Liu et al. (2006c), we define

$$\bar{\mathcal{E}}_0 \equiv (q-1)\mathcal{E}_0 k_{\rm min}^{q-1} \tag{7.10}$$

and a characteristic interaction rate τ_p^{-1} (or its inverse, the characteristic timescale, PL04) that is an indicator of the turbulence intensity

$$\tau_p^{-1} = \frac{\pi}{2}\Omega_{\rm e}\left(\frac{\mathcal{E}_0}{B_0^2/8\pi}\right)(q-1)k_{\rm min}^{q-1} = \frac{\pi}{2}\Omega_{\rm e}\left(\frac{\bar{\mathcal{E}}_0}{B_0^2/8\pi}\right). \tag{7.11}$$

Once the resonance interactions are found and the turbulence spectrum is given, one can proceed to evaluate the **Fokker-Planck coefficients**:

$$D_{ab} = \frac{(\mu^{-2}-1)}{\tau_p\gamma^2}\sum_{j=1}^{N}\chi(k_j) \begin{cases} \mu\mu(1-x_j)^2, & \text{for } ab = \mu\mu; \\ \mu p x_j(1-x_j), & \text{for } ab = \mu p \text{ or } p\mu; \\ p^2 x_j^2, & \text{for } ab = pp, \end{cases} \tag{7.12}$$

where

$$\chi(k_j) = \frac{\mathcal{E}(k_j)/\bar{\mathcal{E}}_0}{|\beta\mu - \beta_g(k_j)|} \quad \text{and} \quad x_j = \mu\omega_j/\beta k_j\,, \tag{7.13}$$

p is the particle momentum, $\beta_g = d\omega/dk$ is the wave group velocity, and the summation over j is for all the possible resonance interactions (the roots found above). Note the F-P coefficients are symmetric, $D_{p\mu} = D_{\mu p}$.

Fokker-Planck Equation Coefficients and Timescales

Finally, we are ready to derive the coefficients in the Fokker-Planck equation. Let us first define two ratios of the F-P coefficients:

$$R_1(\mu,p)=\frac{D_{pp}}{p^2D_{\mu\mu}}\,,\quad R_2(\mu,p)=\frac{D_{p\mu}}{pD_{\mu\mu}}\,. \tag{7.14}$$

We also define the pitch-angle averaged acceleration and scattering times (PL04, cf., Liu, S., Petrosian, & Mason 2006):

$$\tau_{\rm ac} = \frac{p^2}{\bar{D}_{pp}}=\frac{2p^2}{\int_{-1}^{1}d\mu(D_{pp}-D_{p\mu}^2/D_{\mu\mu})}=\frac{2}{\int_{-1}^{1}d\mu D_{\mu\mu}(R_1-R_2^2)}\,, \tag{7.15}$$

$$\tau_{\rm sc} = \frac{1}{2}\int_{-1}^{1}d\mu\frac{(1-\mu^2)^2}{D_{\mu\mu}}\ll L/v\,,\quad \bar{D}_{pp}\equiv\frac{1}{2}\int_{-1}^{1}d\mu(D_{pp}-D_{p\mu}^2/D_{\mu\mu})\,, \tag{7.16}$$

where the factor $2=\int_{-1}^{1}d\mu$ and L is the size of the acceleration region. Note that we assume isotropic pitch-angle distribution here and the R_2^2 term in equation 7.15 should be dropped if isotropy is not satisfied (e.g., Liu, S., Petrosian, & Mason 2006). Accordingly, the diffusion coefficient[2] (Petrosian, 2001) and the direct acceleration rate[3] can be written as

$$D(E) = \beta^2\bar{D}_{pp}=\frac{\beta^2}{2}\int_{-1}^{1}d\mu(D_{pp}-D_{p\mu}^2/D_{\mu\mu}) \tag{7.17}$$

$$= \frac{\beta^2p^2}{\tau_{\rm ac}}=\frac{\beta^2p^2}{2}\int_{-1}^{1}d\mu D_{\mu\mu}(R_1-R_2^2)\,, \tag{7.18}$$

$$A(E) = \frac{1}{\beta\gamma^2}\frac{d\beta\gamma^2D(E)}{dE}-\frac{d}{dE}D(E)=\frac{D(E)}{E}\frac{2-\gamma^{-2}}{1+\gamma^{-1}}\,. \tag{7.19}$$

We also obtain the escape time that combines nonrelativistic and extreme relativistic cases

$$T_{\rm esc}=\frac{L}{\sqrt{2}v}\left(1+\frac{\sqrt{2}L}{v\tau_{\rm sc}}\right), \tag{7.20}$$

and define the direct acceleration time, $\tau_a=E/A(E)$.

Now that all the coefficients, including $D(E)$, $A(E)$, and $T_{\rm esc}$ in the F-P equation have been evaluated, the equation can be solved numerically by the Chang-Cooper method (Park & Petrosian, 1996). In this particular study, we assume a steady state solution (the acceleration code is capable of solving the time-dependent F-P equation though), because the transport code is of steady state and we need a self-consistent treatment throughout. Once

[2]There is a typo in eq. (12) of PL04, where E^2 should be replaced with β^2p^2, but the calculation there was actually correct.

[3]Subtracting the $dD(E)/dE$ term results from the different ways of writing the F-P equation, see eq. (7.1) here and eq. (10) of PL04.

the electron spectrum, $f_{\rm ac}(E)$, in the acceleration region is obtained, we evaluate the *escaping electron flux*

$$F_{\rm esc}(E) = \frac{f_{\rm ac}(E)}{T_{\rm esc}(E)} L\,, \tag{7.21}$$

which is then passed to the transport code as an injection. We can define the ratio between the escape flux and the LT flux ($v f_{\rm ac}$):

$$R_{\rm esc} = \frac{F_{\rm esc}}{v f_{\rm ac}} = \frac{L}{v T_{\rm esc}} = \sqrt{2}\left(1 + \frac{\sqrt{2}L}{v\tau_{\rm sc}}\right)^{-1}. \tag{7.22}$$

The equivalent *thick-target electron flux* (Petrosian & Donaghy 1999; PL04) is calculated by:

$$F_{\rm thick}(E) = \frac{\beta c}{\dot{E}_L}\int_E^\infty \frac{f_{\rm ac}(E')}{T_{\rm esc}(E')} dE'. \tag{7.23}$$

7.2.2 Particle Transport and Radiation Model

The next step is to run the **transport code** that follows the electron distribution as the electrons stream down the newly reconnected magnetic field line and travel through different layers of the atmosphere. In order to run the transport code, we need the knowledge of two things. The first is the energy and pitch-angle distribution of the injected particles, which is given above as the escaping electron flux (assumed isotropic in the forward direction) by the acceleration code. The second is the background density and abundance distribution along the loop. Here we assume a fully ionized, pure hydrogen plasma,[4] whose distribution is taken from the result of the HD code (see below).

The transport code solves the fully relativistic, steady-state, F-P equation (see eq. (1) in McTiernan & Petrosian, 1990), which includes Coulomb energy loss (no energy diffusion)[5] and pitch-angle diffusion, synchrotron energy loss and pitch-angle diffusion, as well as magnetic field convergence. Following McTiernan (1989), we neglect the return current (Syniavskii & Zharkova, 1994; Zharkova et al., 1995), which is a good approximation if the electron flux is sufficiently small; we hope to include this effect in the future to achieve a more self-consistent treatment. The variable[6] to be solved is the electron flux spectrum $F(E, s, \mu)$ as a function of energy E, distance s from the injection point (at the boundary

[4] Although this assumption is not self-consistent with the abundance assumed in the acceleration code, it simplifies the calculation of the Coulomb logarithm (assume $\ln\Lambda = 20$) which is needed for evaluating the Coulomb loss. This assumption will only affect the normalization in the resulting electron flux as well as the photon emission very slightly. Again, this makes room for future improvement.

[5] We again assume a cold background plasma here, which is a good approximation for solar flares, particularly because accelerated particles lose most of their energy in the cold chromosphere. However, in principle, particles could gain energy as well by colliding with background particles when their velocities are smaller than those of the background ones, and thus Coulomb diffusion in energy should be included in the future (see more discussion in Chapter 10).

[6] The code actually solves for $F(E, s, \mu)/\beta^2 = cf(E, s, \mu)A(s)/(\beta A_0) \equiv c\Phi A(s)/A_0$, where Φ is the same as that defined in (McTiernan & Petrosian, 1990).

of the acceleration region), and pitch-angle cosine μ. It is evaluated as

$$F(E,s,\mu) = \frac{1}{A_0}\int c\beta f(E,s,\mu)dA(s) = c\beta f(E,s,\mu)\frac{A(s)}{A_0} \tag{7.24}$$

where $f(E,s,\mu)$ is the density distribution function in units of electrons $\mathrm{cm}^{-3}\,\mathrm{keV}^{-1}\mathrm{sr}^{-1}$ (cf. $f_{\rm ac}(E)$ in the acceleration code which is integrated over all pitch angles), and we integrate the differential electron flux $c\beta f(E,s,\mu)$ over the cross-sectional area $A(s)$ of the loop and then divide it by a constant equivalent area A_0. Thus $F(E,s,\mu)$ (a real physical flux) has units of electrons $\mathrm{s}^{-1}\,\mathrm{cm}^{-2}\,\mathrm{keV}^{-1}\mathrm{sr}^{-1}$ (in the code, $\mathrm{keV}^{-1}\mathrm{sr}^{-1}$ is replaced with per $m_e c^2$ per unit pitch-angle cosine). The (angle integrated) injection from the acceleration code serves as the boundary condition at $s = 0$, namely,

$$F(E,s,\mu)|_{s=0} = F_{\rm esc}(E)/2\,, \tag{7.25}$$

where the factor $2 = \int_{-1}^{1} d\mu = \cos 0 - \cos\pi$ is the range of the pitch-angle cosine. During the steady state calculation, we also set a symmetric boundary condition at the injection site, where particles running away from the domain is reflected back to the loop with identical energy but opposite pitch-angle cosine.

Once we know the electron distribution at all the depths, we calculate the thin-target nonthermal **bremsstrahlung radiation** intensity, $I(\epsilon,s)$, as a function of photon energy ϵ and distance s. $I(\epsilon,s)$, emitted by a unit length along the loop, is integrated over the loop cross-sectional area $A(s)$ and has units of photons $\mathrm{s}^{-1}\,\mathrm{cm}^{-1}\,\mathrm{keV}^{-1}$,

$$I(\epsilon,s) = A_0\int_{\epsilon}^{\infty} dE\left[n_p(s)\frac{d\sigma}{d\epsilon}\int_{-1}^{1} d\mu F(E,s,\mu)\right]\,, \tag{7.26}$$

where $n_p(s)$ is the proton number density[7] ($n_p = n_e$ in our case) and $d\sigma/d\epsilon$ is the angle-averaged[8] differential bremsstrahlung cross-section given by Koch & Motz (1959). The looptop (LT) emission is evaluated as

$$I_{\rm LT}(\epsilon) = A_0\int_{\epsilon}^{\infty} dE\left[n_p(0)\frac{d\sigma}{d\epsilon}\right] c\beta f_{\rm ac}(E)\,, \tag{7.27}$$

where $n_p(0) = n_p(s)|_{s=0} = n_{p,\rm ac}$ is the proton density and $c\beta f_{\rm ac}(E)$ is the angle-integrated electron flux, both in the acceleration region. The equivalent footpoint (FP) photon spectrum is calculated by averaging the intensity below the transition region, located at distance of $s = s_{tr}$

$$I_{\rm FP}(\epsilon) = \frac{1}{s_{max} - s_{tr}}\int_{s_{tr}}^{s_{max}} I(\epsilon,s)ds\,. \tag{7.28}$$

Both $I_{\rm LT}(\epsilon)$ and $I_{\rm FP}(\epsilon)$ can be compared with HXR observations, say, obtained by the *Yohkoh* and *RHESSI* satellites. If the coronal density is negligibly tenuous and if the

[7] In general, n_p should include H^+ as well as protons in He^{++} and other ions.

[8] Angle-dependent radiation will be included in the future (see Chapter 10)

chromospheric density is sufficiently high, $(s_{max} - s_{tr})I_{\rm FP}(\epsilon)$ would approach the thick-target spectrum

$$I_{\rm thick}(\epsilon) = \int_0^\infty I(\epsilon, N) dN \,, \tag{7.29}$$

where $dN = n_p ds$ is the column depth.

7.2.3 NRL Hydrodynamic Model

The NRL Solar Flux Tube Model (MEL89) assumes a two-fluid plasma composed of electrons and ions that can only move along the magnetic field in a flux tube, due to the line-tying condition in a low-β environment. The user-specified geometry (e.g., vertical or semi-circular) of the tube is characterized by $A(s)$, the cross-sectional area of the tube as a function of distance s, and $g(s)$, the component of the gravitational acceleration in the direction of the magnetic field. The model solves the one-dimensional equations of mass, momentum, and energy conservation,

$$\frac{\partial \rho}{\partial t} + \frac{1}{A(s)} \frac{\partial}{\partial s}[A(s)\rho v] = 0, \tag{7.30}$$

$$\frac{\partial}{\partial t}(\rho v) + \frac{1}{A(s)} \frac{\partial}{\partial s}[\rho v^2 A(s)] = \rho g - \frac{\partial P}{\partial s}, \tag{7.31}$$

$$\frac{\partial U}{\partial t} + \frac{1}{A(s)} \left\{ \frac{\partial}{\partial s} A(s) \left[(E + P)v - \kappa_e \frac{\partial T_e}{\partial s} - \kappa_i \frac{\partial T_i}{\partial s} \right] \right\} = \rho v g - L_{\rm rad} + S, \tag{7.32}$$

$$\frac{\partial}{\partial t} \left(\frac{P_e}{\gamma - 1} \right) + \frac{1}{A(s)} \left[\frac{\partial}{\partial s} A(s) \left(\frac{\gamma v P_e}{\gamma - 1} - \kappa_e \frac{\partial T_e}{\partial s} \right) \right] = -L_{\rm rad} + S + \gamma_{\rm eq}(T_i - T_e), \tag{7.33}$$

where ρ is the mass density, v is the fluid velocity, and $P = P_e + P_i$ is the total pressure, a combination of the electron pressure P_e and the ion pressure P_i, which are given by the equations of state

$$P_e = n_e k_{\rm B} T_e \quad \text{and} \quad P_i = n_i k_{\rm B} T_i \,, \tag{7.34}$$

where $k_{\rm B}$ is the Boltzmann constant, n_e and T_e (n_i and T_i) are the electron (ion) number density and temperature, respectively. Here, the combined kinetic and thermal energy is given by

$$U = \frac{1}{2}\rho v^2 + \frac{P}{\gamma - 1} \,, \tag{7.35}$$

where $\gamma = 5/3$ is the ratio of specific heats; κ_e and κ_i are the electron and ion thermal conductivities, respectively,

$$\kappa_e = 1.1 \times 10^{-6} T_e^{5/2} \,, \quad \kappa_i = \kappa_e / 25 \,; \tag{7.36}$$

$L_{\rm rad} = n_e n_p \Phi(T_e)$ is the radiative energy loss rate (MEL89), where n_p is the hydrogen number density and $\Phi(T_e)$ is the optically-thin radiative loss function; S is the heating rate,

$$S = S_0 + S_e \,, \tag{7.37}$$

where S_0 is the background heating, set to be $8.31 \times 10^{-3}\,\mathrm{ergs\,s^{-1}\,cm^{-3}}$ (MEL89), presumably caused by coronal heating in the quiet sun active region, and S_e is heating by nonthermal electrons, which will be provided by the Fokker-Planck transport model in this study. $\gamma_{\rm eq} = 1.4 \times 10^{-17} n_e^2 T_e^{-3/2}$ is the rate coefficient for electron-ion temperature equilibration; in this particular study, we assume $T_e = T_i$ and thus the $\gamma_{\rm eq}(T_i - T_e)$ term vanishes. We also assume that the plasma consists of fully ionized hydrogen. The electron and ion number densities, n_e and n_i, are then related to the mass density by

$$n_e = \frac{\rho Z}{\mu m_p (1+Z)} \quad \text{and} \quad n_i = n_e/Z\,, \tag{7.38}$$

where $Z = 1.0$ is the mean ionic charge and $\mu = 0.5$ (in units of proton masses m_p) is the mean mass[9] per particle.

The hydrodynamic equations are solved by a finite difference scheme. The code uses time-step splitting, in which the hydrodynamic calculation takes place first, using the Flux Corrected Transport (FCT) method, and then the implicit part of the code takes care of thermal conduction and radiation. Note that there is no physical or artificial viscosity in this model, but the FCT achieves similar effects to stabilize the calculation as artificial viscosity usually does and make conservative physical quantities actually conserved in the meantime. Because of lacking of viscosity, hydrodynamic waves, once excited, can exist for a long duration with little or no damping, as we will see in Chapter 9. A reflective (or symmetric) boundary condition is imposed at both the top (loop apex) and bottom (deep into the chromosphere) boundaries. Details of the numerical scheme and the model parameters can be found in Mariska et al. (1982) and MEL89.

7.2.4 Combining the Particle and Hydrodynamic Codes

We now describe how we combine the flare particle code and the NRL HD code. Since the two codes are independent and mature on their own rights, there is no need to rewrite a whole new code that includes functionality of both. Rather, one would like to have a wrapper that can coordinate between the two codes and have them communicate while running independently on each side. By doing so, one can keep each code essentially intact and self-contained. Fortunately this is possible because the communication between the two codes could be as simple as passing back and forth a 1D array. As we noted above, in order to determine the electron distribution at each depth, the transport code needs the background density profile that can be provided by the HD code. On the other hand, the HD code needs to know how much energy[10] is deposited by the accelerated electrons as a function of distance, which can be obtained from the particle transport calculation. Then this energy deposition rate (or electron heating rate) will work as a driver for the hydrodynamics, which will change the density distribution, which, in turn, will be fed back to the particle code. We detail below how to implement this approach.

[9] In the original model of MEL89, the plasma consists of fully ionized hydrogen and helium with the helium assumed to be 6.3% of the hydrogen by number density, corresponding to $Z = 1.059$ and $\mu = 0.5724$. This minor difference would only affect the mass normalization here slightly.

[10] We neglect the momentum exchange between accelerated electrons and the background particle, which is a valid approximation because of electron's small mass. See Chapter 10 for a discussion on future work.

Electron Heating Rate and Thermal Conduction

As we noted in §7.1, the **heating rate** is critical in HD simulations, but was not calculated properly in previous works. Here we improve on this by calculating the electron energy loss directly from the electron distribution obtained from the transport calculation, with two equivalent approaches.

The electron heating rate S_e (in units of $\mathrm{ergs\,s^{-1}\,cm^{-3}}$), as defined in the HD equations (see eq. [7.37]), is equal to the energy deposition rate in a unit volume by fast electrons. It can be evaluate from the energy loss rate $\dot{E}_{\rm Coul}$ (due to Coulomb collisions) as

$$S_e(s) = \int_{E_{\rm min}}^{E_{\rm max}} dE \int_{-1}^{1} f(E,s,\mu)\dot{E}_{\rm Coul} d\mu\,, \tag{7.39}$$

where $[E_{\rm min}, E_{\rm max}]$ is the range of the energy bins used, $\dot{E}_{\rm Coul}$ is given by equation (7.3), the electron distribution function $f(E,s,\mu)$ can be obtained from the corresponding electron flux $F(E,s,\mu)$ via equation (7.24).

Alternatively, one can calculate the (net downward) energy flux carried by the electrons

$$F_{\rm erg}(s) = \frac{A_0}{A(s)} \int_{E_{\rm min}}^{E_{\rm max}} dE \left[\int_0^1 \mu E F(E,s,\mu) d\mu - \int_{-1}^{0} \mu E F(E,s,\mu) d\mu \right], \tag{7.40}$$

and differentiate it to obtain the net energy gain in a unit volume

$$S_e(s) = dF_{\rm erg}(s)/ds\,, \tag{7.41}$$

where $\mu E F(E,s,\mu)$ is the energy flux projected (by the factor μ) along the loop the factor $A_0/A(s)$ accounts for the variation of the cross-sectional area. This approach is, in practice, equivalent to the above one (eq. [7.39]), because, in the deka keV to hundreds of keV energy range, the combination of synchrotron loss and bremsstrahlung HXRs only constitutes a negligible fraction ($\lesssim 10^{-4}$) of the total energy loss due to Coulomb collisions. We took the second approach in our simulation, and let the transport code calculate the heating rate and pass it to the HD code.

As to **thermal conduction**, we use the usual Spitzer conductivity without suppression, unlike what we do for the decay phase (see Chapter 9). This is because, during the impulsive phase, in addition to direct turbulence heating (believed to be present in the turbulence or acceleration region), there is significant acceleration taking place. The energized particles can escape and carry energy away from the acceleration region, which serves as a energy "conduction" channel. In contrast, during the decay phase, acceleration already subsides, and heating and suppression of conduction due to turbulence is the main energization agent. In addition, strong turbulence during the impulsive phase might act differently from weak turbulence in the decay phase. These arguments, however, are speculative and more in-depth investigation is required in the future.

Code Communication Timescale

Ideally, the flare particle code and the hydrodynamic code should work interactively and communicate at every time step during the time advance. Unfortunately, although we have a

time-dependent acceleration code, the transport code is of steady state and it would require extensive programming to upgrade it to a time-dependent version. However, fortunately, under certain assumptions, the required programming work can be significantly simplified and reasonably good accuracy can be achieved.

Our approach is to have the two codes communicate at certain intervals. Each communication consists of two parts. The first part is that the HD code passes the density profile to the flare particle code. Then the flare code runs a full *steady state* calculation from acceleration of particles, to the particle transport and bremsstrahlung radiation. Then it comes the second part of the communication, in which the flare code passes the electron heating rate (energy deposition) to the HD code. The HD code then runs its own time-dependent calculation until the next communication. Then two questions arise: (1) what is the optimum timescale for the two code to communicate; (2) what heating rate function should be provided to the HD code between adjacent communications. We address these below.

(1) The **communication timescale** should not be shorter than that on which a steady state particle transport calculation is valid. The timescale in the electron transport process can be expressed in terms of the lifetime τ_e of electrons. It is determined by the energy loss (mainly due to Coulomb collisions for nonrelativistic electrons) time in a given magnetic loop geometry and the atmospheric condition. For a low-energy electron, the Coulomb loss time is relatively short, but it would take relatively longer time for the electron to reach the dense transition region where it can lose most of its energy. The opposite is true for a high-energy electron. A combination of these factors results in the lifetime $\tau_e(E)$, which depends on the electron energy E and the atmospheric structure. For example, Petrosian (1973, see eq. (9) and Fig. 1 there) assumed a gravitationally stratified atmosphere with a scale height of $H = kT/mg$, and obtained $\tau_e(E)$ as a function of E for nonrelativistic electrons. $\tau_e(E)$ has a maximum (at some critical energy $E_{\rm cr}$) which is (eq. (11) in Petrosian, 1973)

$$\tau_{e,\,\max}(H, n_e) \approx 0.07\,\sec \left(\frac{H}{10^8\,\rm cm}\right) \left(\frac{n_e H}{10^{18}\,\rm cm^{-2}}\right)^{-1/4}, \tag{7.42}$$

where n_e is the electron number density at the injection site. For timescales greater than $\tau_{e,\,\max}$, it is reasonable to assume a steady state solution for the F-P transport equation. To be conservative, if we take the coronal temperature to be $T = 10^6$ K and the density at the acceleration region to be $n_e = 10^{10}\,\rm cm^{-3}$, we obtain $\tau_{e,\,\max} = 1.5$ s at $E_{\rm cr} = 65$ keV. On the other hand, if one assumes a constant coronal density of $n_e = 10^{10}\,\rm cm^{-3}$ and an exponential rise of density (with a scale height of $H = 603\,$km, given $T \approx 10^4\,$K in the chromosphere) starting at the transition region, then the required time is

$$t_e = l/v + \tau_{e,\max}(H, n_e) \lesssim 0.1\,\sec \left(\frac{l}{10^9\,\rm cm}\right) \left(\frac{E}{25\,\rm keV}\right)^{-1/2} + 0.05\,\sec\,, \tag{7.43}$$

where l is the length of the coronal portion of the loop, the electron velocity v is evaluated with the non-relativistic approximation, and $\tau_{e,\max}(H, n_e) = 0.05\,$s (at $E_{\rm cr} = 6.5$ keV) is obtained from equation (7.42). For a loop of $l = 10^4\,$km and an electron of $E = 25\,$keV, such a timescale is $t_e \lesssim 0.15\,$s. We therefore take a conservative $\Delta t = 2\,$s as the time interval for the two codes to communicate.

(2) Since the $\Delta t = 2\,\mathrm{s}$ interval is much shorter than the HD response time[11], **between adjacent communications**, we assume that the energy deposition by nonthermal electrons as a function of column depth $S_e(N)$ (in units of $\mathrm{ergs\,s^{-1}\,cm^2}$, where $\mathrm{cm^2}$ means per unit column depth) is constant in time. This is true (i) if we neglect energy losses (synchrotron and bremsstrahlung) other than Coulomb loss, which is valid for X-ray producing electrons (energy range from tens of keV to hundreds of keV); and (ii) if the loop cross-sectional area $A(s)$ is a constant, i.e., a uniform loop. We have made the code meet these two conditions. Then the spatial distribution of the heating rate $S_e(s,t)$ varies with time only according to the redistribution of density and the variation of column depth as a function of distance,

$$S_e(s,t) = S_e(N) n_e(s,t)\,. \tag{7.44}$$

This means that at each time t, for a given distance s, we first identify its corresponding column depth $N(s,t) = \int_0^s n_e(s,t)ds$, then use this $N(s,t)$ to evaluate the heating rate $S_e(N)$, and finally multiply $S_e(N)$ with the local density to convert the units from $\mathrm{ergs\,s^{-1}\,cm^2}$ to $\mathrm{ergs\,s^{-1}\,cm^{-1}}$ (because $S_e(s)ds = S_e(N)dN$ and $dN = n_e ds$).

Summary of Communication: Task Flow Chart

Figure 7.1: Task flow chart for Particle & HD code communication

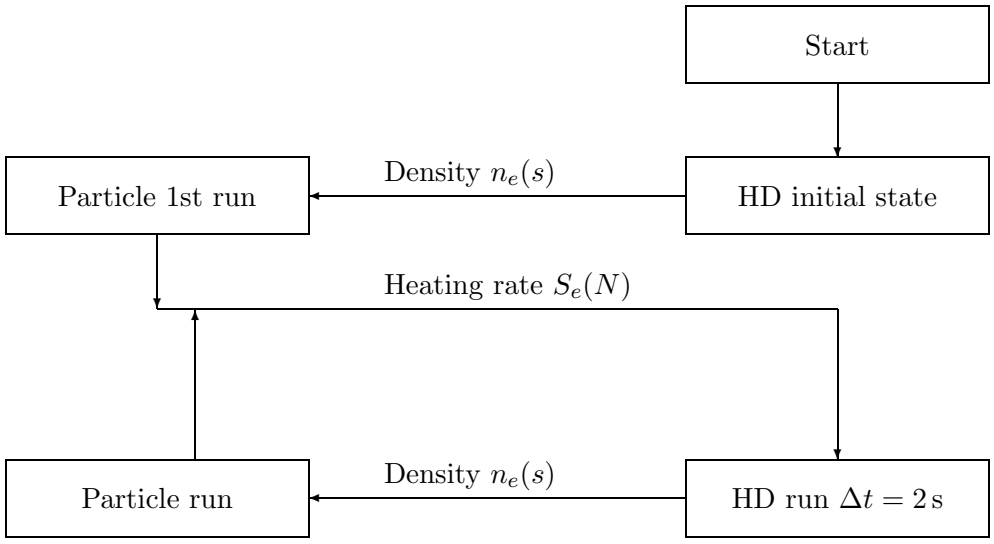

[11] This can be characterized by the sound travel time, which is about 60 s in a coronal loop of 10^4 km long with a temperature of $T = 10^6$ K (sound speed $c_s = 166\,\mathrm{km\,s^{-1}}$).

Let us now summarize the communication between the two codes with the following task flow chart. At the beginning of the simulation, the HD code passes its initial density distribution to the particle code. Based on this density profile, the particle code runs its first steady state calculation and returns the heating rate $S_e(N)$ as a function of column depth N to the HD code. Now the HD code takes this heating rate and converts it to a function of distance, $S_e(s)$, at each time step using the current density profile. While doing so, the HD code advances a time interval of $\Delta t = 2\,\mathrm{s}$, and then passes the updated density distribution back to the particle code again. This finishes a full cycle of calculation and next cycle starts over from the particle calculation again.

7.3 Simulation Result

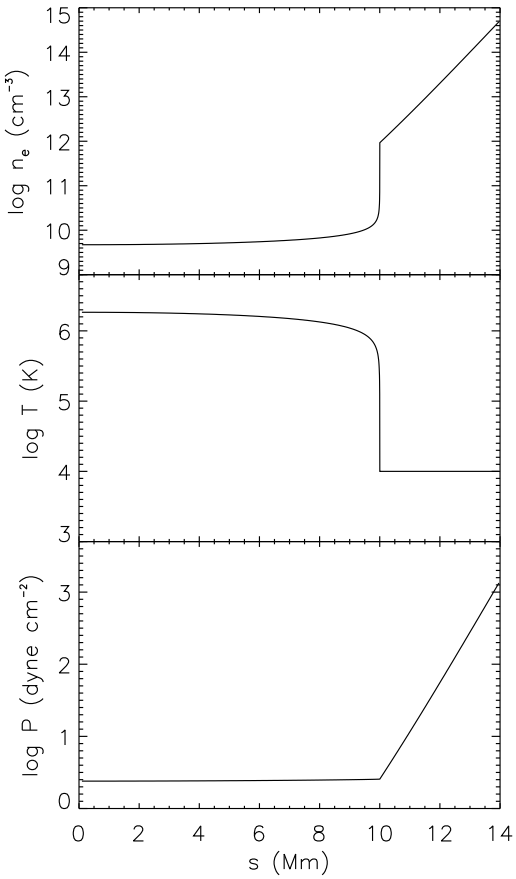

Figure 7.2: Initial state of the flare loop for the HD simulation. Distance starts from the LT where particles escape from the acceleration region.

Figure 7.2 shows the initial hydrostatic state of the plasma in one half of the loop (assumed to be symmetric), which displays the electron number density, temperature, and gas pressure vs. distance. We have a hot coronal region with $T \gtrsim 10^6\,\mathrm{K}$ and a transition

region (TR) at around $s = 10\,\mathrm{Mm}$ where T quickly drops to the chromospheric value of $10^4\,\mathrm{K}$. The density, on the contrary, increases with distance from the tenuous ($< 10^{10}\,\mathrm{cm}^{-3}$) coronal portion, experiences a sharp jump at the TR, and reaches close to $10^{15}\,\mathrm{cm}^{-3}$ at the bottom ($\sim 4\,\mathrm{Mm}$ below the TR) of the simulation domain.

From the same initial state, we have run five cases using different heating model parameters (which are summarized in Table 7.1). For each case, we use the identical loop geometry as MEL89 (see Chapter 9). We take a linear ramp in time for the normalization of the electron heating, with a rise of 30 s followed by a decline of another 30 s. After the first 60 s of impulsive phase calculation, we continue the simulation well into the decay phase until $t = 90\,\mathrm{s}$. We describe each of the simulation cases in the rest of this section, focusing on the evolution of the hydrodynamics and the energy and spatial distribution of the accelerated electrons and bremsstrahlung photons. We defer our investigation on the energy budget and the Neupert effect test of these case to next chapter.

7.3.1 Case R: Reference Calculation

It is instructive to run the first case with the original model of MEL89 and use it as a reference for comparing new results from our model. We use almost identical parameters as the "Reference Calculation" case in MEL89: spectrum index $\delta = 6$ and "knee" energy $E_1 = 15\,\mathrm{keV}$. The only two differences are: (1) here the "peak beam flux",[12] i.e., parameter F in equation (9) of MEL89, is $2.67 \times 10^{10}\,\mathrm{ergs\,cm^{-2}\,s^{-1}}$, while they used $5 \times 10^{10}\,\mathrm{ergs\,cm^{-2}\,s^{-1}}$; (2) we assume a fully ionized hydrogen plasma while they included helium which constitutes 6.3% of hydrogen number density.

The evolution of the flaring plasma is shown in Figure 7.3. We plot electron number density n_e, temperature T, gas pressure P, upward velocity v, energy deposition rate S_e, radiative loss rate L_{rad}, and heat conduction flux F_{cond} at selected times during the first 60 s of simulation. The plasma exhibits the same general evolution as that in Figure 1 of MEL89, which we briefly account as follows. As is evident, electron beam heating (S_e), which acts as the driver of the simulation, is concentrated in the upper chromosphere just below the transition region and heating in the corona is negligible early in the simulation. Heat conduction also carries energy that is deposited in the corona by nonthermal electrons down to the upper chromosphere, but this energy flux is overwhelmed by direct beam heating, particularly on the early stage of the flare. This localized beam heating, although counteracted by radiative loss that appears to be co-spatial, quickly heats chromospheric plasma, produces overpressure, and drives mass upflow. A downflow (with a velocity down to $-115\,\mathrm{km\,s^{-1}}$) in a narrow region of the chromosphere is also present to counterbalance the upward moment. Such a downflow is usually observed in blueshifted SXR or EUV line spectrum. The downward momentum produced by electron heating could be partly responsible for photospheric seismic waves observed during major flares (Kosovichev & Zharkova, 1998; Kosovichev, 2006).

At $t = 10\,\mathrm{s}$, the upflow velocity exceeds $100\,\mathrm{km\,s^{-1}}$ and a discontinuity or an evaporation front[13] has already developed near the transition region (see the n_e panel). It travels upward

[12] cf., the actual energy deposition flux in Table 7.1.

[13] The discontinuity is not necessarily a shock if the Rankine-Hugoniot (RH) relations are not satisfied. We have not checked the RH relations since we are not concerned with such detailed gas dynamics here.

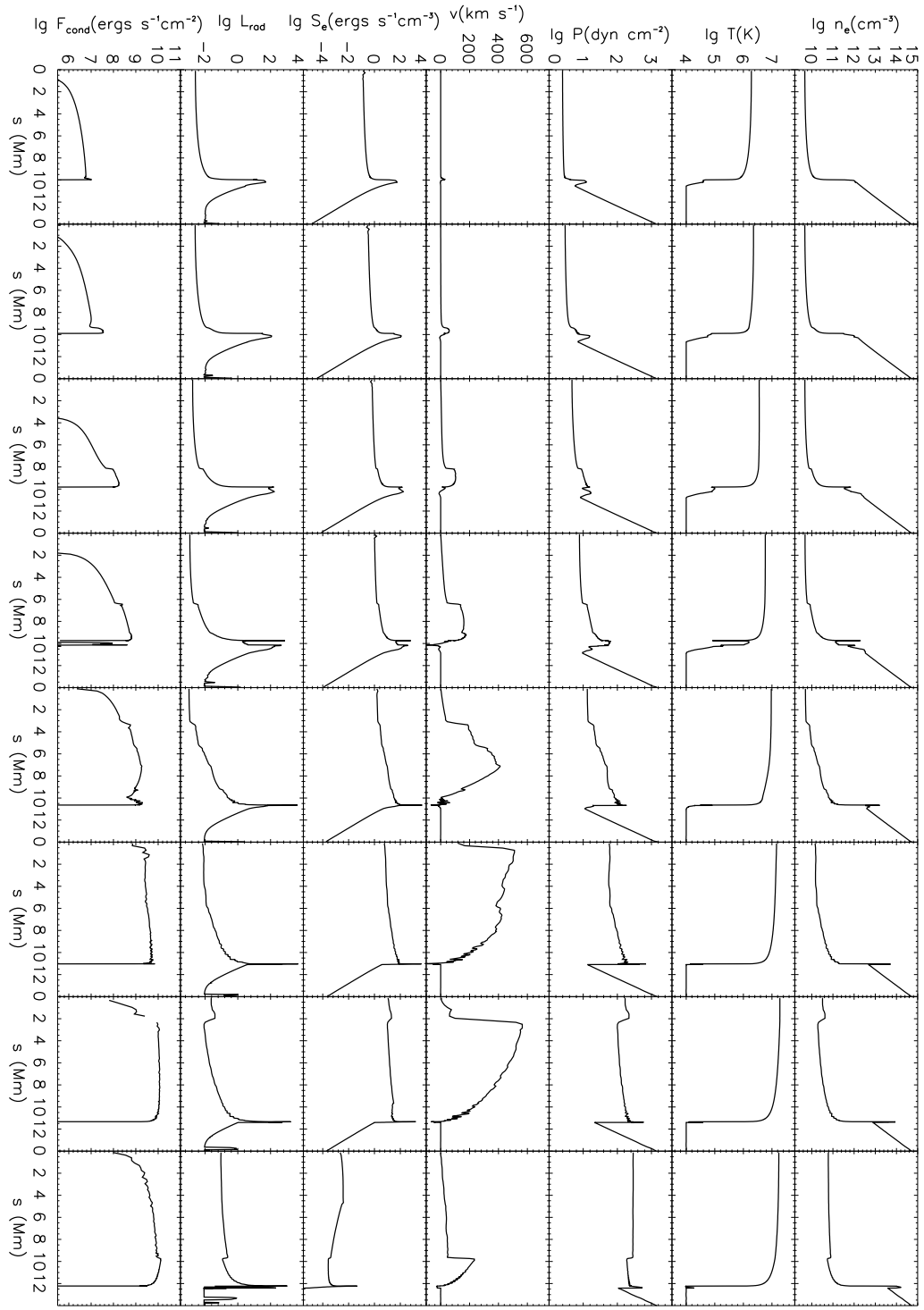

Figure 7.3: Evolution of electron density, temperature, pressure, upward velocity, energy deposition rate S_e, radiative loss rate $L_{\rm rad}$ (in same units as S_e), and heat conduction flux $F_{\rm cond}$ for Case R.

and reaches the loop apex at $\sim 29\,\mathrm{s}$. It is then reflected back and material piles up there due to the reflective boundary condition imposed. This reflection can be understood as plasma flow from the other end of the loop in a symmetric loop geometry where there is no acceleration region present in the middle of the loop; or it can be assumed to be due to the encountering of the plasma with the acceleration region boundary where the upflow is stuck by strong turbulence, if we assume a geometry with an acceleration region sitting near the LT. The upflow reaches its maximum velocity of $565\,\mathrm{km\,s^{-1}}$ at $\sim 35\,\mathrm{s}$, which is delayed by 5 s from the maximum energy deposition at $t = 30\,\mathrm{s}$. The strength of evaporation subsides afterwards, but the coronal density continues to rise through the end of the simulation.

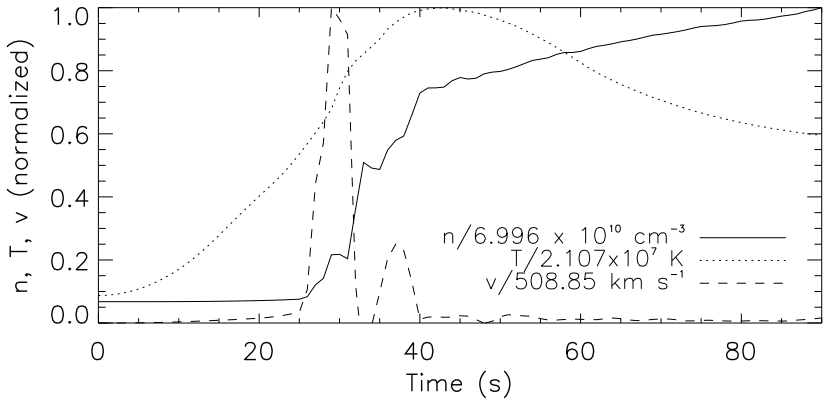

Figure 7.4: History of various quantities (electron number density, temperature, and upward velocity) at 1 Mm from the LT for Case R. Each variable is normalized to its maximum, as shown in the legend. The density curve have two sharp jumps, one followed by the other. The first jump is due to the arrival of the evaporation front from *below*, and the second one comes about because of the reflection of the front at the loop apex (coming from *above*).

We can also inspect the plasma evolution by following the temporal variation of a physical quantity at a position fixed in space. Figure 7.4 shows the history of electron number density, temperature, and velocity at $s = 1\,\mathrm{Mm}$ (in the corona) from the loop apex. As can be seen, the density and velocity stay almost constant until $\sim 25\,\mathrm{s}$ when the evaporation front arrives and produces a sudden jump. The second jump in density results from the evaporation front reflection. In contrast, the temperature varies much smoother. It attains its maximum of $2.11 \times 10^7\,\mathrm{K}$ at $t = 44\,\mathrm{s}$ and decreases monotonically since then because conductive cooling overtakes beam heating at this position in the loop.

7.3.2 Case A: Fiducial Run with SA Model

We used the same parameters for acceleration as in PL04 (see their Fig. 12), i.e., $\tau_p^{-1} = 70\,\mathrm{s^{-1}}$, $n_e = 1.5 \times 10^{10}\,\mathrm{cm^{-3}}$, $B = 400\,\mathrm{G}$, $k_BT = 1.53\,\mathrm{keV}$, and the acceleration region size $L = 5 \times 10^8\,\mathrm{cm}$. The peak rate of particle injection was set at $Q_0 = 5.73 \times 10^{11}$electrons $\mathrm{s^{-1}\,cm^{-3}}$ to provide a peak energy deposition flux of $2.56 \times 10^{10}\,\mathrm{ergs\ s^{-1}\,cm^{-2}}$ similar to that of Case R. We chose 200 energy bins uniformly spaced in the logarithmic space that covers the range of $[10^{-3}, 10^3] \times 511$ keV. There are 24 pitch-angle bins set in the

transport code, with 12 uniform bins symmetrically spanning each half of the $[0, \pi]$ range ($0 \leq \theta < \pi/2$ and $\pi/2 < \theta \leq \pi$; note $\theta \neq \pi/2$). We modulate the injection rate $Q(t, E)$ linearly in time, with a 30 s rise followed by a 30 s decay.

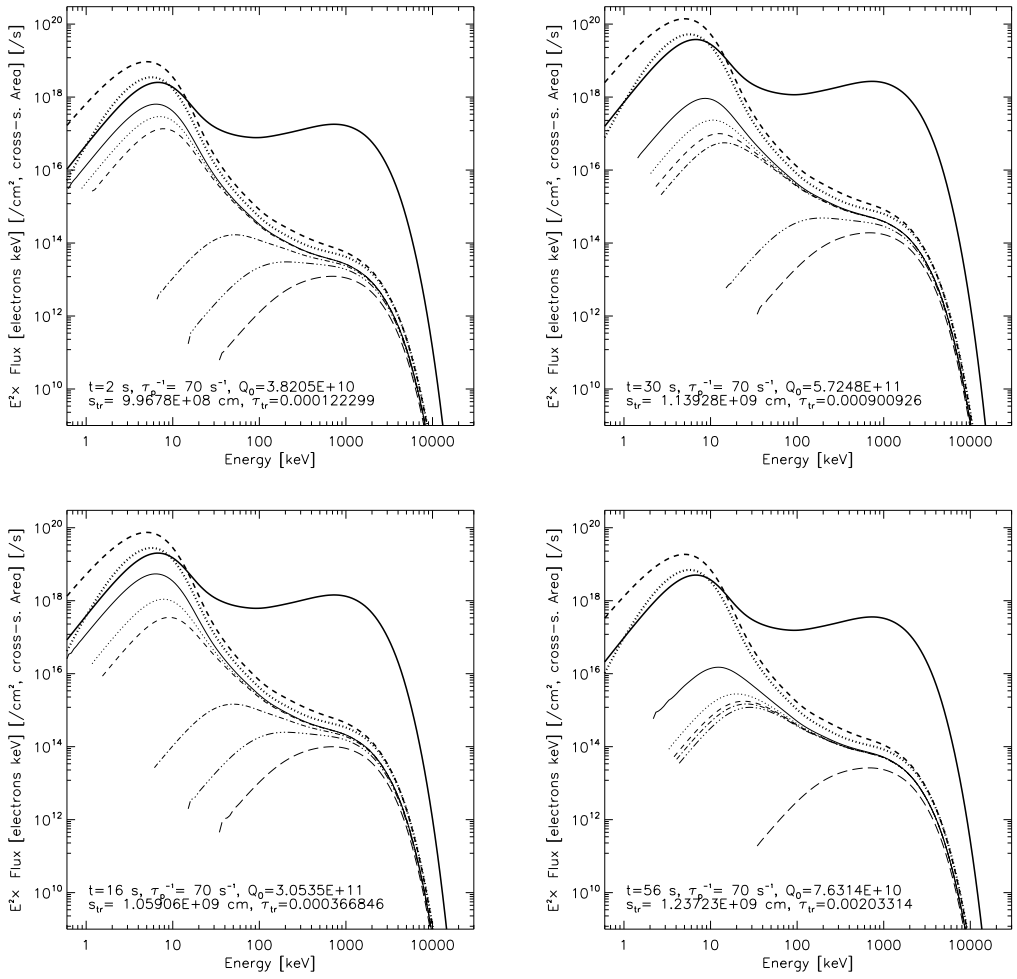

Figure 7.5: Evolution of $E^2F(E)$ spectra for Case A, where $F(E)$ is the angle-integrated electron flux. The thick dashed, dotted, and solid lines indicate the LT, escaping, and equivalent thick-target electron flux, respectively. The thin lines (from top to bottom: *solid*, *dotted*, *dashed*, *dot-dashed*, *triple-dot–dashed*, and *long-dashed*) are for the spectrum at distances of $s = 4$, 8, 10, 11, 12, and 13 Mm from the injection site at the LT, respectively. The legend includes the current values of τ_p^{-1}, the particle injection rate Q_0 (in units of electrons $\mathrm{s}^{-1}\,\mathrm{cm}^{-3}$), and the distance ($s_{\mathrm{tr}}$) and column depth ($\tau_{\mathrm{tr}}$, in units of $5 \times 10^{22}\,\mathrm{cm}^{-2}$) from the LT to the transition region.

The $E^2F(E)$ electron flux spectrum [where $F(E) = f(E)\beta c$ is the angle-integrated electron flux] at the LT (*thick dashed line*) is shown in Figure 7.5. It contains a quasi-thermal portion at low energies and a nonthermal tail at high energies, with a smooth transition in between (PL04). It does not invoke any artificial low-energy cutoff or energy break. This particular spectrum shape is consistent with observed HXR spectra that can

often be fitted with an isothermal plus power-law model. Since the acceleration parameters (e.g., τ_p^{-1}) are set constant in time, this spectrum does not change in shape, but does vary in normalization. The thick dotted line indicates the electron flux escaping from the acceleration region, which is the input to the transport code and acts as a driver to the electron-beam heated HD evolution. We describe the plasma evolution below and defer a discussion of the corresponding particle transport and radiation effects afterwards.

HD Evolution

Figure 7.6 shows the evolution of the plasma in the loop. As we can see, the general evolution is similar to that of Case R, though much faster. The evaporation front reaches the loop apex at $t = 22\,\mathrm{s}$ (instead of 29 s in Case R), the maximum upflow velocity of $627\,\mathrm{km\,s^{-1}}$ is attained at $t = 22\,\mathrm{s}$ (instead of $565\,\mathrm{km\,s^{-1}}$ at $t = 22\,\mathrm{s}$ in Case R), and the maximum coronal temperature is 2.61 K (2.11 K in Case R).

These differences are a consequence of the spatial distribution of the energy deposition S_e, which first decreases (while it increases in Case R) with distance from the LT and then increases and peaks just below the transition region. In addition, the peak of the S_e curve in the chromosphere is relatively narrower than that in Case R, which means a comparably smaller fraction of energy is directly deposited in the chromosphere. This is because the electron spectrum here (Fig. 7.5) has a smooth continuous distribution including the high-energy nonthermal regime and the low-energy quasi-thermal regime. There is a significant portion of the total energy content that resides in low-energy electrons. These electrons give up most of their energy to the coronal portion of the loop, resulting in significant coronal heating. The coronal temperature thus increases rapidly and produces a relatively sharp temperature gradient and large heat conduction flux (see panels at $t = 2\,\mathrm{s}$ and $t = 5\,\mathrm{s}$). We note that the peak of the conduction flux, which is close to the LT at the beginning ($t = 2\,\mathrm{s}$), shifts downward and reaches the transition region at $t = 9\,\mathrm{s}$ when the upflow velocity rises sharply and exceeds $100\,\mathrm{km\,s^{-1}}$. In this sense, the evaporation is driven more by conduction than by direct heating. As evaporation develops and the coronal density increases, the coronal fraction of the energy deposition increases as well and dominates over the chromospheric portion on the late stage.

In contrast, the spectrum adopted in MEL89 is a power-law ($\delta = 6$) with a low-energy cutoff at $E_1 = 15\,\mathrm{keV}$ below which the electron spectrum has a positive index of 2. This spectrum has its peak at 15 keV and electrons of this energy are stopped in the chromosphere where they lose most of their energy, where the radiative loss (which acts like a sink in the energy transfer) is most efficient. This means that a significant part of energy deposited by beaming electrons is quickly radiated away (also see Fig. 8.2 and text there) in situ in the upper chromosphere and a smaller fraction of energy is available to evaporate chromospheric material than in Case A. Note that the conductively driven scenario in Case A has energy input into the transition region and produces evaporation, which occurs slightly above the radiatively-efficient layer in the upper chromosphere. This makes conductively-driven evaporation more efficient and results in higher upflow velocity and higher coronal temperature and density, as can also be seen in Figure 7.19.

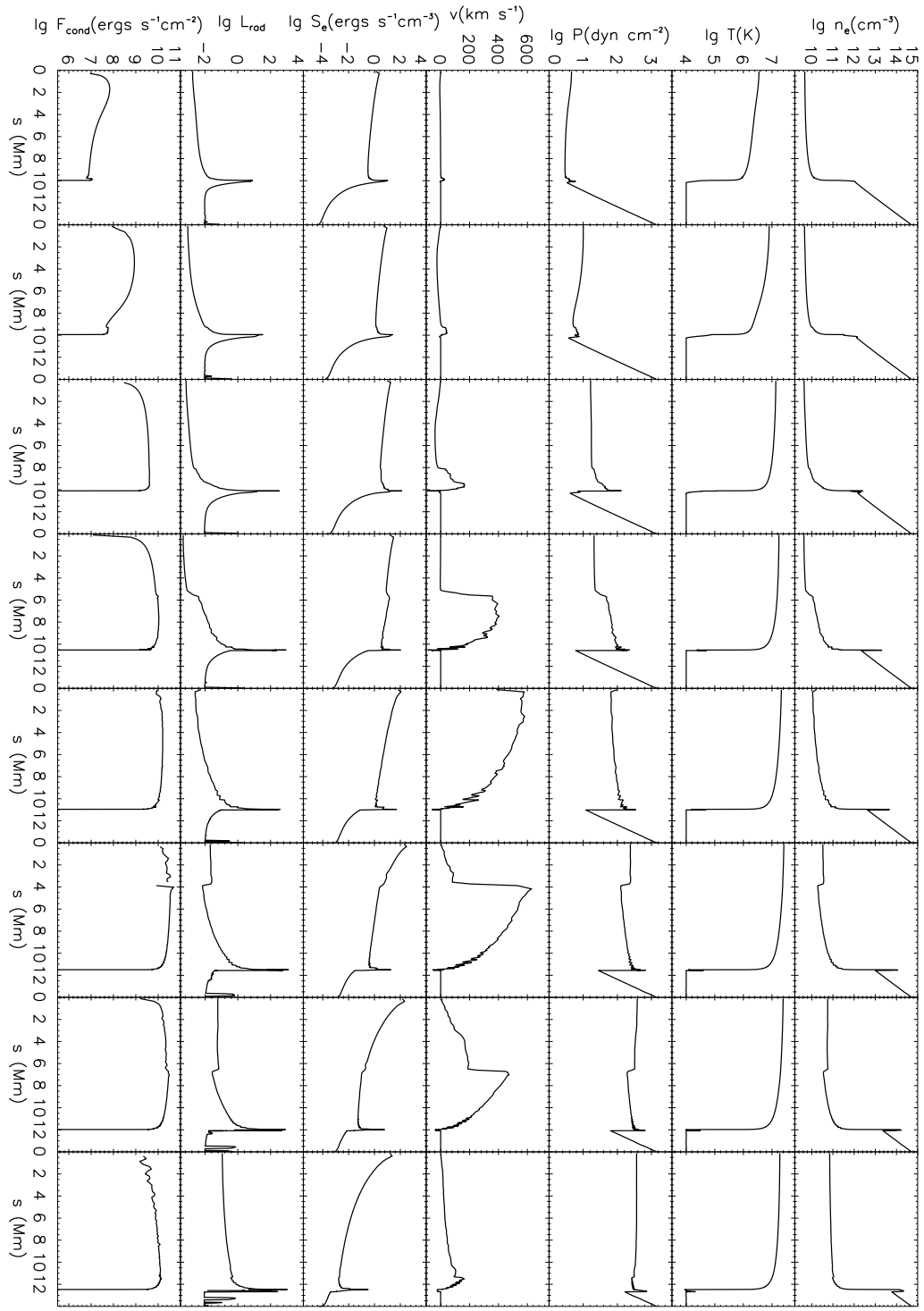

Figure 7.6: HD evolution of various quantities for Case A, similar to Fig. 7.3.

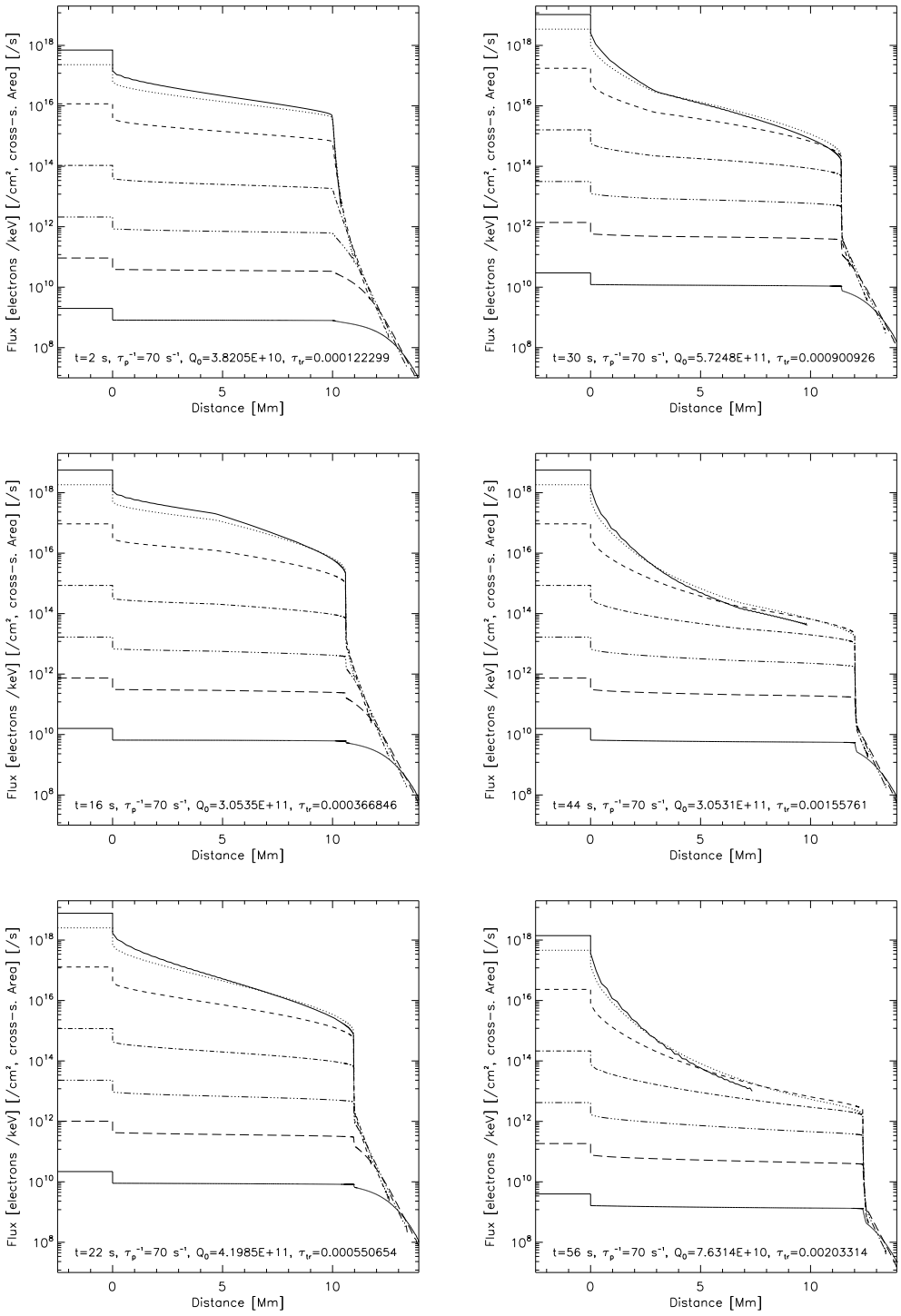

Figure 7.7: Evolution of electron flux vs. depth at different energies for Case A. From top to bottom, the curves correspond to electron energies of 3.1, 6.1, 12.3, 24.5, 48.8, 97.4, and 294.1 keV, respectively. The steps in the region of negative distance denote the average electron flux ($f_{\rm ac}(E)\beta c$) in the acceleration region, one half of whose length is shown here.

Evolution of Electron Distribution

Figure 7.5 shows the evolution of **electron flux spectrum** at different locations in the loop. The thick solid line represents the equivalent thick-target electron flux (see eq. [7.23]). As expected, it appears to be much harder than the LT flux in the 10–1000 keV range. The broken gray-scale lines (from top to bottom) are for spectra at $s = 4$, 8, 10, 11, 12, and 13 Mm from the LT injection site. Early into the flare ($t = 2\,\mathrm{s}$), the transition region is located at $s = 9.97\,\mathrm{Mm}$ and its column depth $\tau = 1.22 \times 10^{-4}$ (in units of $5 \times 10^{22}\,\mathrm{cm}^{-2}$). At this time, the top two gray-scale lines (solid and dotted) indicate spectra in the corona, which are very similar to the escape flux because of small column depths from the injection site. The other four gray-scale lines are spectra below the transition region, which, as expected, become harder with an increasing deficit of low-energy electrons as column depth increases. This is because only high-energy electrons can penetrate deep into the chromosphere.

In this simulation case, because the LT spectrum shape does not change with time (so does the escape flux and thick-target flux), the spectrum at a particular column depth should also remain constant in shape and only vary in normalization. However, as time progresses, evaporation takes place and the height of the transition region drops, while the coronal density increases. This causes variations with time of the column depth (and the electron spectrum) at each position in space. This is just what we see here. At $t = 56\,\mathrm{s}$, for example, the transition region shifts down to $s = 12.4\,\mathrm{Mm}$ at a column depth of $\tau = 2.02 \times 10^{-3}$. In the lower-right panel of Figure 7.5, only one chromospheric spectrum is left, and the other (coronal) spectra are very alike because they are exposed in the corona and their column depths are very close.

We can also check the electron **flux distribution vs. distance** at different energies, which is shown in Figure 7.7. We also display the flux in the acceleration region (LT) for comparison as the region of negative distance. In general, the electron flux decreases with distance from the injection site. The slope of these curves is steeper for low energy electrons than that for high-energy electrons because low-energy electrons lose energy faster (due to the $1/\beta$ dependence of Coulomb loss rate). The flux drops much steeper in the chromosphere (than in the corona) because of its high density and thus large column depth per unit distance. This produces a break in the curve around the transition region and wherever a sharp density change occurs. At $t = 16\,\mathrm{s}$, for example, a break near $s = 5\,\mathrm{Mm}$ is obvious for electron energies of 3.1 and 6.1 keV. This is actually where the evaporation front is located. At $t = 22\,\mathrm{s}$, because the evaporation front already reaches the apex of the loop and the density in the whole loop has increased significantly, the electron flux distribution is much steeper than before in the whole coronal portion. Similar evaporation signatures are present throughout the duration of the flare (see the right column of Fig. 7.7).

Evolution of Bremsstrahlung Radiation

Figure 7.8 shows the bremsstrahlung **photon spectra** at different depths that are produced by the accelerated electrons discussed above (see the corresponding Fig. 7.5). Likewise, the LT photon spectrum (*thick dashed*) also shows a thermal-like component in the low-energy range. It hardens in the intermediate energy range and softens again to the high-energy end. The FP spectrum (*thick solid*) is much harder (than the LT spectrum), and in the range from tens of keV to a few hundred keV, it mimics the commonly observed power-law

FP spectrum. As distance increases, the spectrum (*thin lines*) becomes harder because the electron spectrum has the same trend of variation.

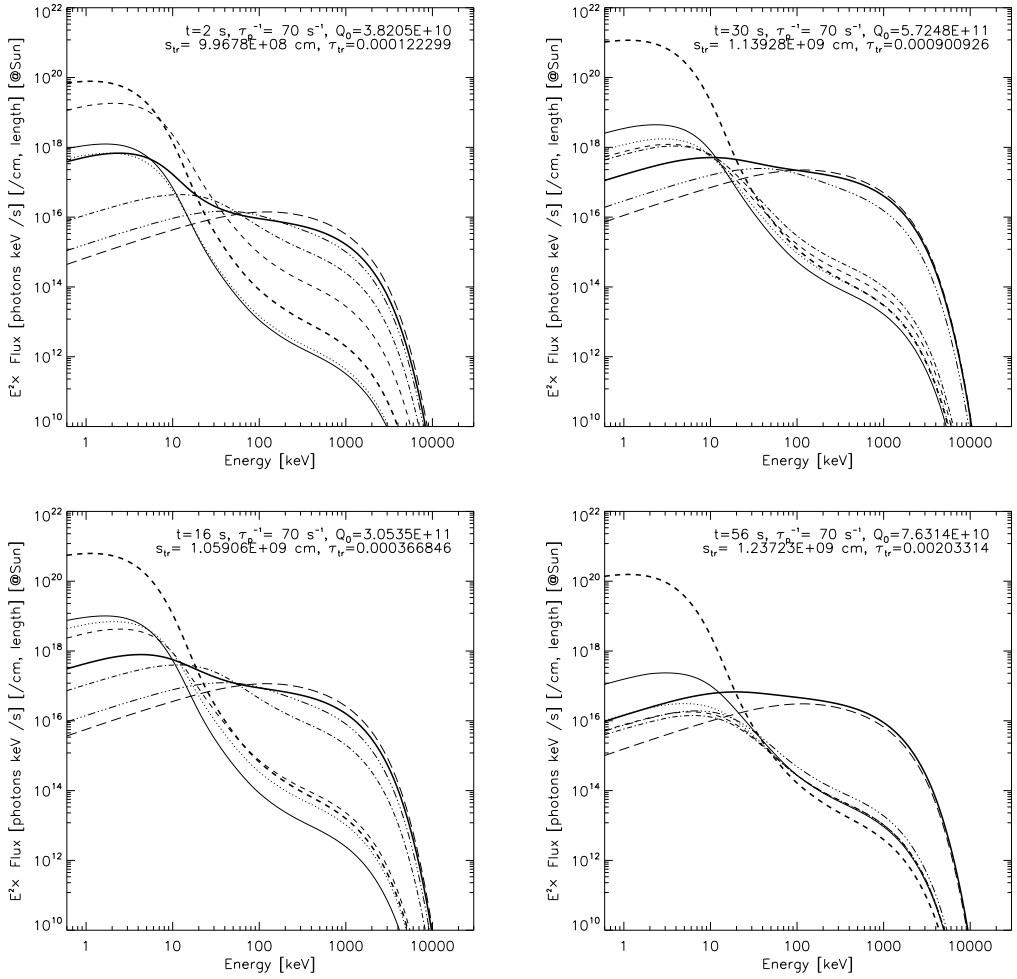

Figure 7.8: Evolution of νF_ν photon spectra at different locations for Case A. The spectrum is of photons emitted by a unit length of the loop, integrated over the loop cross-sectional area. The thick dashed line indicates the LT spectrum, and the thick solid line is the averaged spectrum below the transition region, which is analogous to observed FP spectra. The thin lines, same as those in Fig. 7.5, are for distances s = 4, 8, 10, 11, 12, and 13 Mm from the LT.

Note that, at $t = 2s$, the two coronal spectra (*thin solid* and *dotted*, close to the LT spectrum in shape) are lower than the first chromospheric spectrum (*thin dashed*) at all energies. This is because early in the course of the flare, the coronal density is low and thus the bremsstrahlung production there is at a low level too. As evaporation develops and the coronal density increases, the photon spectrum in the upper-corona portion ($s \leq 8\,\mathrm{Mm}$) of the loop becomes harder because the electron spectrum there hardens. At the same time, as more and more volume of the loop turns into the corona (since the transition region drops), some locations previously buried in the chromosphere are now exposed in the corona. These

locations have lower (than before) column depth and thus softer electron spectrum, which produces softer photons spectrum as well. This can be seen from the evolution of the three spectra at s= 10, 11, and 12 Mm in Fig. 7.8. At $t = 56$ s, all the thin-lined spectra (except the long-dashed line) are from coronal locations and they appear alike in both shape and normalization simply because the density differences among these locations are now much smaller than before.

The **spatial distribution** of the photon emission at different energies (same as in Fig. 7.7) is plotted in Figure 7.9. On the early stage of the flare evolution, low-energy emission comes primarily from the LT, while high energy emission is concentrated below the transition region. Because the bremsstrahlung radiation is proportional to the product of the electron spectrum and the local proton density, the photon emission profile can reveal more details of the density distribution than the electron flux profile (Fig. 7.7). As is evident, the emission profile follows the density features (including the evaporation front and the density spike at the transition region, see Fig. 7.6) very well. As the flare develops and evaporation continues, more and more emission comes from the coronal portion of the loop. At low energies, the emission drops with distance much steeper than before in the corona due to the dramatic density increase there. At intermediate energies, we find a temporal transition from FP-dominated emission to LT-dominated emission. At very high energies, such a change is not present because even the high density corona is still more or less transparent for high energy electrons. However, the retreat of the transition region down to chromospheric heights is visible in all the emission profiles.

We should bear in mind that all the emission features described here are not necessarily observable given the current technology and spatial resolution of the active space missions. However, it is worth trying to make a comparison with observations. As shown in Chapter 6, in the 2003 November 13 flare, we identified an XR emission feature that shifts from the FP toward the LT with time. In this simulation case, we also find the bremsstrahlung XR emission tracks the evaporation front. At low energies, e.g., $E = 3$ keV, there is a local brightness enhancement at the evaporation front due to the sharp jump of density and thus increased bremsstrahlung productivity. Such a local brightness blob can exceeds the FP intensity (spatially integrated and averaged) and is comparable to the LT intensity. In principle, this blob could be imaged by *RHESSI* and could be responsible for the observed moving source. Note that at high energies, although the evaporation front is also visible in the HXR emission profile, its intensity is dwarfed by the FP emission and thus is not observable due to limited dynamic ranges of the instruments (e.g., 10 for *RHESSI*). On the other hand, thermal emission from the heated and evaporated plasma could also contribute to low energy X-rays, and such contributions could be comparable at certain energies. Of course, as photon energy increases, the thermal emission drops quickly due to its exponential decay with energy; and thus thermal contribution at high energies are negligible compared with nonthermal emission. At what photon energy thermal and nonthermal emissions are comparable? Answers to this question depends on the electron spectrum, as well as the density and temperature distribution of the thermal plasma. It would be interesting to check the relative importance of thermal vs. nonthermal emission and their spatial distribution, with different model parameters. Unfortunately, such a study would be beyond the scope of the current investigation.

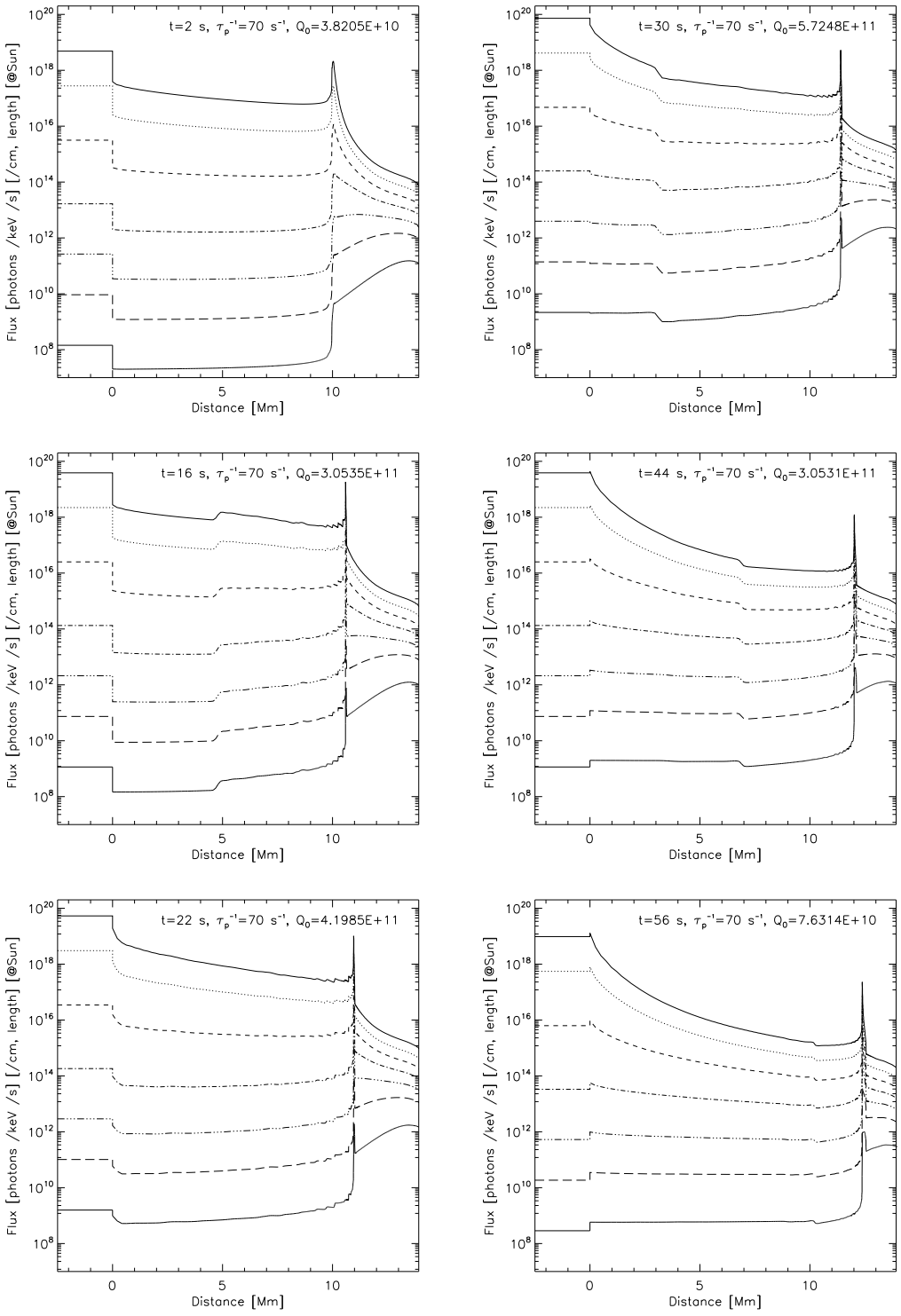

Figure 7.9: Evolution of photon emission vs. depth at different photon energies of Case A. As in Fig. 7.7, the energies are 3.1, 6.1, 12.3, 24.5, 48.8, 97.4, and 294.1 keV.

7.3.3 Case B: Variable Electron Spectrum

This is the second simulation case using the combine particle and HD code. In addition to the time modulation of the spectrum normalization, we vary the acceleration rate τ_p^{-1} linearly with time, in the same triangular pattern. This means that the electron spectrum experiences a *soft-hard-soft* variation, as is commonly observed in solar flares (Grigis & Benz, 2004), and can be seen here.

Figure 7.10 shows the evolution of the **electron spectra** at different depths. Clearly, at the beginning ($t = 0\,\mathrm{s}$) when there is very little acceleration ($\tau_p^{-1} = 2.33\,\mathrm{s}^{-1}$), the spectra at all the depths look similar to the injected thermal distribution (not shown) which has a sharp exponential cutoff. Note that some electron spectra at large depths are too small to appear in the plot due to the extreme softness of the spectrum and the resulting sharp decrease of electron flux with distance. As time proceeds and the acceleration rate increases, the spectrum becomes harder and harder, particularly in the energy range of $[10, 10^3]$ keV. At $t = 30\,\mathrm{s}$, the thick-target flux exhibits a hump with a positive slope. Meanwhile, the quasi-thermal component at the low-energy end is present all the time. After the peak time of 30 s, spectrum softening takes place and the spectrum shape returns to that of the quasi-thermal one in the end. The corresponding photon spectra (Fig. 7.11) show the same trend of soft-hard-soft variation. Other spectrum (of both electrons and photons) variations (such as those due to chromospheric evaporation) are similar to those of Case A.

Figure 7.12 shows the evolution of the electron flux (*left*) and photon intensity (*right*) **vs. distance** at different energies, which is similar to that of Figures 7.7 and 7.9, respectively. One of the main differences is that electron spectrum here is soft on the early and late stages, and consequently the plot spans a wide range on the vertical scale.

Another spectrum feature that makes Case B different from Case A is the **escaping electron flux**. As we can see from Figure 7.10, on the early and late stages of the flare when the acceleration rate is low, the escape flux (*thick dotted*) and the LT flux (*thick dashed*) are almost identical above $\sim 10\,\mathrm{keV}$; below such an energy, their difference increases with decreasing energy. Around the acceleration rate peak time (similar in Case A), such an critical energy shifts to $> 10^3$ keV. This is because the escape flux is inversely proportional (eq. [7.21]) to the escape timescale, $T_{\rm esc}$, which depends on the scattering timescale $\tau_{\rm sc}$ through equation (7.20). From equations (7.22), (7.16), and (7.12), we see the escape-to-LT electron flux ratio $R_{\rm esc}$[14] is a decreasing function of the acceleration rate τ_p^{-1}. When τ_p^{-1} is low and the scattering timescale $\tau_{\rm sc}$ is large, at a given energy, $R_{\rm esc}$ would be relatively large. Because of this, there are relatively more electrons that escape the acceleration region and deposit their energy into the loop in Case B than in Case A, since here τ_p^{-1} has a triangular time profile with its peak value equal to that of Case A (which is constant in time there). We find the mean energy deposition flux here is $9.8 \times 10^{10}\,\mathrm{ergs\,s^{-1}\,cm^{-2}}$, while in Case A it is $8.3 \times 10^{10}\,\mathrm{ergs\,s^{-1}\,cm^{-2}}$ (also see Table 7.1). Since this case has a larger energy input rate, we would expect stronger chromospheric evaporation here, which we discuss below.

Let us now check the corresponding **HD evolution**, which is shown in Figure 7.13 At the very beginning, because very little acceleration takes place and the spectrum is very soft, the energy deposition curve drops sharply (cf., Case A) with depth into the chromosphere.

[14]The functional (vs. E) form of $R_{\rm esc}(E)$ would depends on that of $T_{\rm esc}(E)$ or $\tau_{\rm sc}(E)$. See Figs. 11 and 12 in PL04.

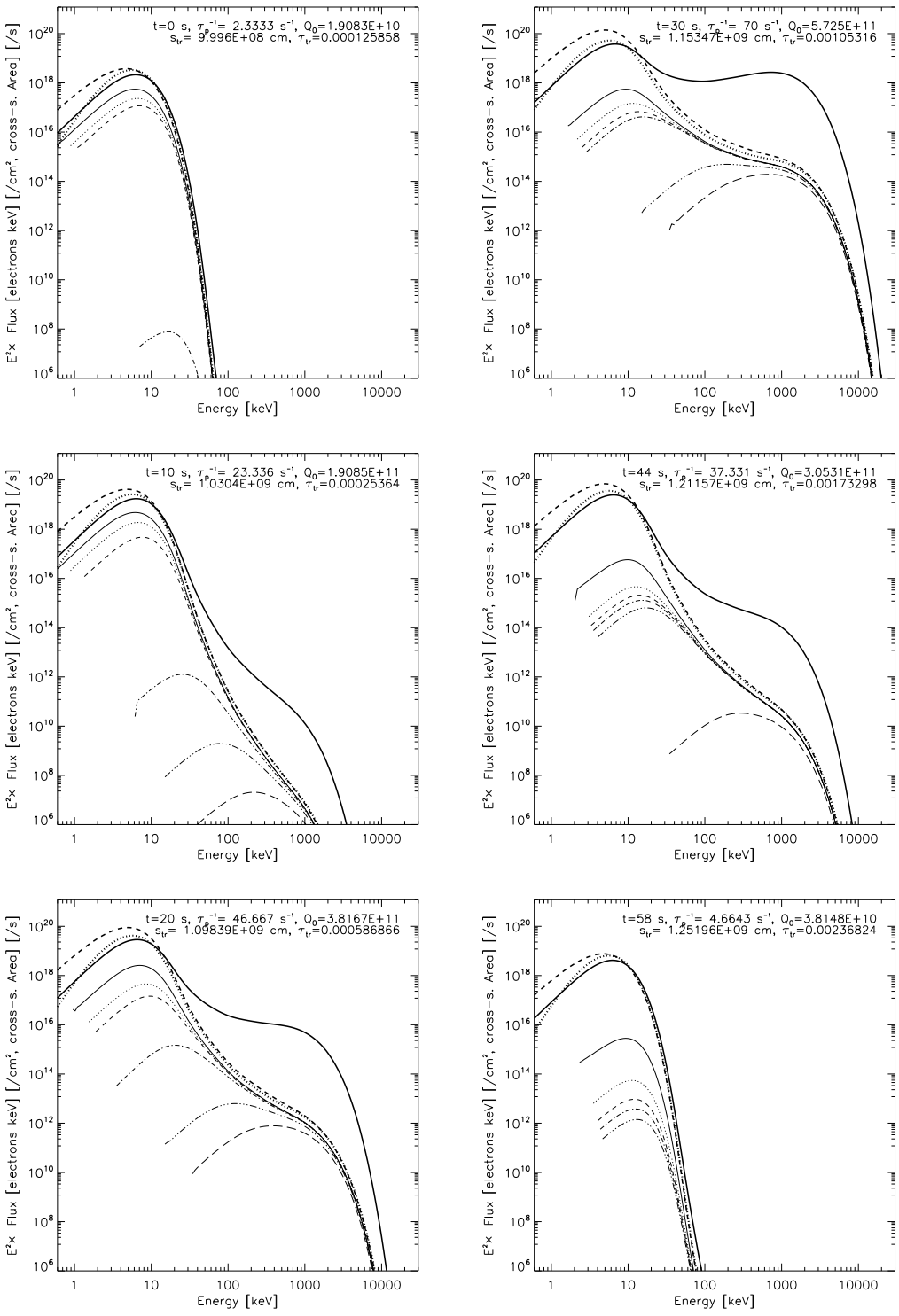

Figure 7.10: Same as Fig. 7.5 (electron spectra at different depths), but for Case B. Note that at $t = 0\,\mathrm{s}$, some spectra at large depths ($s > 10\,\mathrm{Mm}$) are too small to be shown.

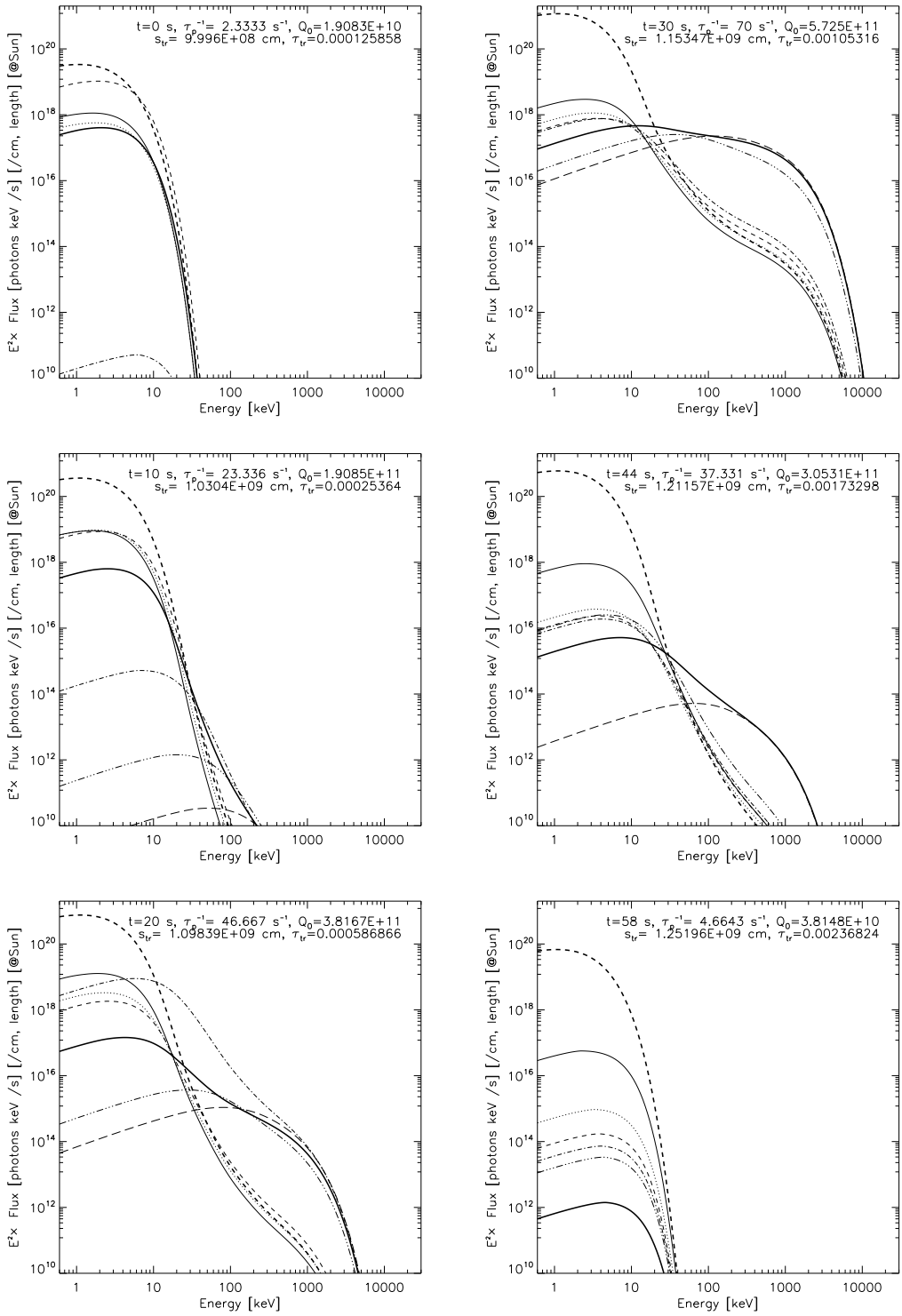

Figure 7.11: Same as Fig. 7.8 (evolution of photon spectra at different depths), but for Case B.

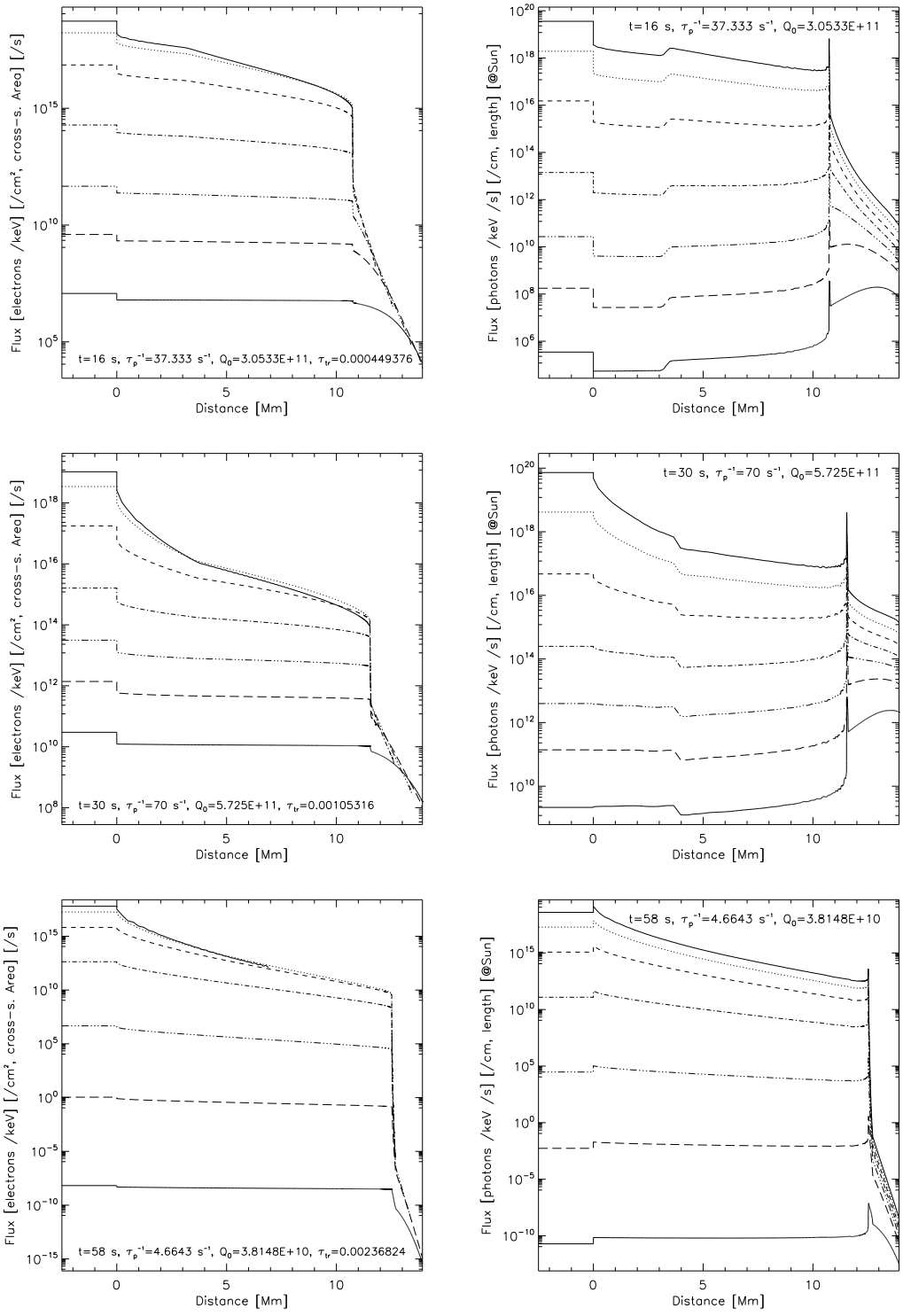

Figure 7.12: Evolution of electron (*left*) and photon (*right*) fluxes vs. distance at different energies (same as Figs. 7.7 & 7.9) for Case B. Time goes from top to bottom (note different vertical scales).

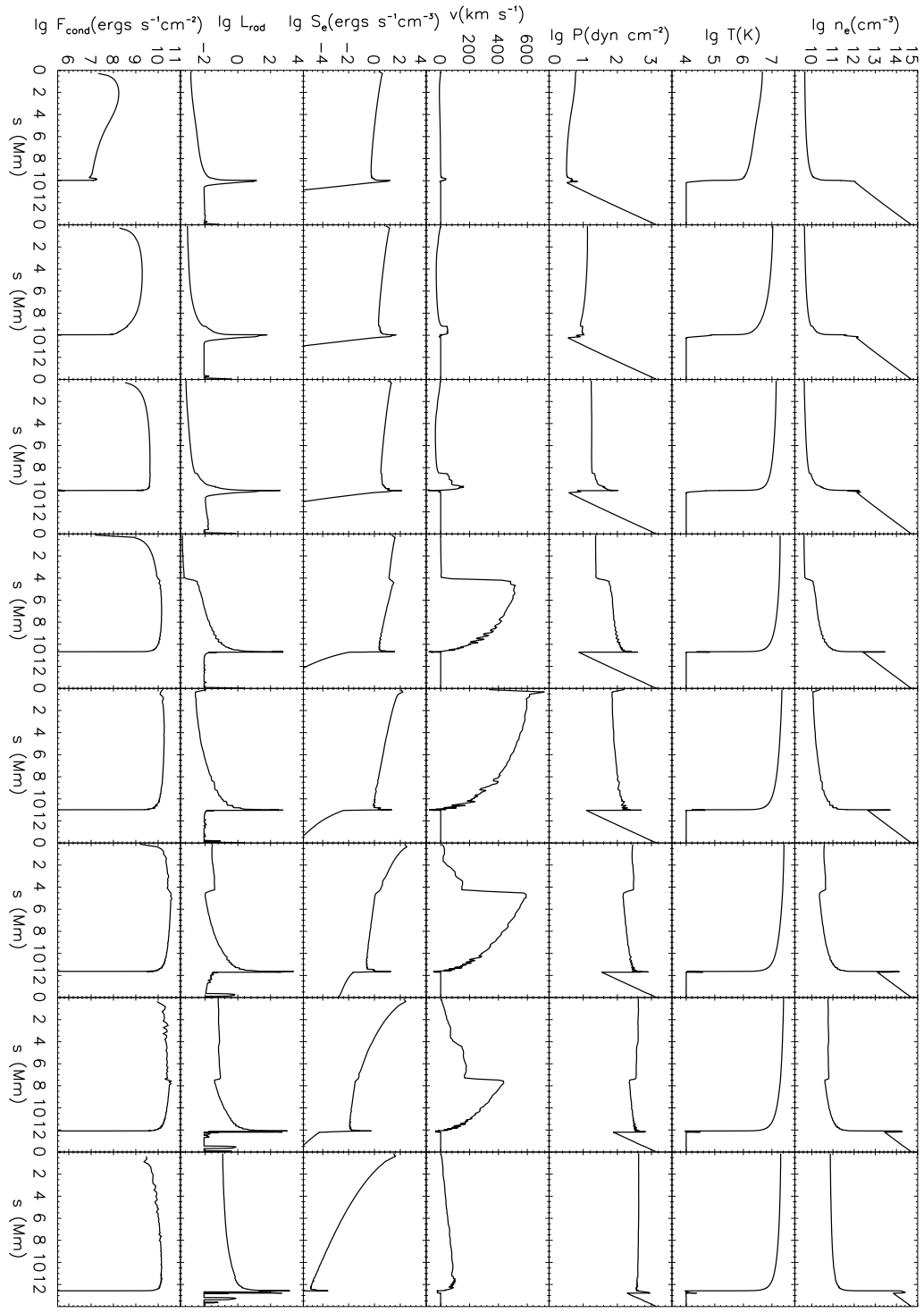

Figure 7.13: HD evolution of various quantities for Case B.

As noted earlier, low-energy electrons are more efficient at heating the corona and we would expect that the softer spectrum, on top of the larger escaping electron flux discussed above, will generally result in stronger coronal heating. This is just the case in this run, which shows a faster evolution and more dramatic evaporation than Case A. At $t = 7\,\mathrm{s}$ (vs. 9 s in Case A), the peak conduction has already reached the transition region and upflow velocity has become greater than $100\,\mathrm{km\,s^{-1}}$. At $t = 20\,\mathrm{s}$ (cf., 22 s in Case A) the evaporation front is reflected at the loop apex and at the same time the upflow attains its maximum velocity of $718\,\mathrm{km\,s^{-1}}$ (cf., $627\,\mathrm{km\,s^{-1}}$ at $t = 32\,\mathrm{s}$ in Case A). This case has also the highest values of maximum downflow velocity, maximum coronal temperature and density out of the five cases under study (see Table 7.1).

7.3.4 Case C: Harder Electron Spectrum

In this case, we set $\tau_p^{-1} = 100\,\mathrm{s^{-1}}$, which means higher rate of acceleration, and we would expect harder electron spectrum than Case A ($\tau_p^{-1} = 70\,\mathrm{s^{-1}}$). This is true as can be seen from the electron and photon spectra shown in Figure 7.14. Compared with Case A, the electron (*left*) flux also decreases with distance slightly slower and the photon (*right*) distribution shows relatively more emission coming from below the transition region than in the corona (see Fig. 7.15). The normalization of HXR emission[15] is also much higher than that of Case A, again, because the harder electron spectrum here has a higher bremsstrahlung yield (see, e.g., Fig. 6.11).

Another effect of the larger acceleration rate is the relatively smaller flux of escaping electrons that enters the loop. Although there are more electrons in the high-energy portion of the spectrum (thus more energy content there), most of the energy is still contained in the low-energy electrons because of the steepness of the spectrum). Therefore, the addition of energy due to more accelerated high-energy particles is relatively small, and it loses to its competing factor, i.e., the smaller escape flux, which produces a smaller overall energy flux input to the loop than Case A.

We note from Figure 7.16 that the energy deposition rate decreases slower with distance in the corona and beyond the transition region, particularly in the late phase of the flare, than that in Case A. This is due to the harder spectrum we have here, which produces slightly less coronal heating and more chromospheric heating. In addition, the relatively smaller escaping electron flux here results in less energy flux. For the same reasons discussed above, as opposed to Case B, we would also expect slightly weaker evaporation and slower evolution of the plasma, which is the case (see Table 7.1 and Figs. 7.19 and 7.16). For example, the maximum coronal temperature and density are $2.48 \times 10^7\,\mathrm{K}$ and $7.84 \times 10^{10}\,\mathrm{cm^{-3}}$, respectively, which is on the order of 10% lower than those in Case A. MEL89 reached a qualitatively similar conclusion by using a harder ($\delta = 4$, vs. 6) power-law spectrum.

7.3.5 Case D: Smaller Normalization

In the last case, we used smaller normalization of $Q_0 = 5.73 \times 10^{10}\mathrm{particles\,s^{-1}\,cm^{-3}}$, which is about one order of magnitude smaller than the fiducial Case (A). This change is

[15]The spatially integrated HXR light curve and its normalization can be seen in Fig. 8.11 of next chapter too.

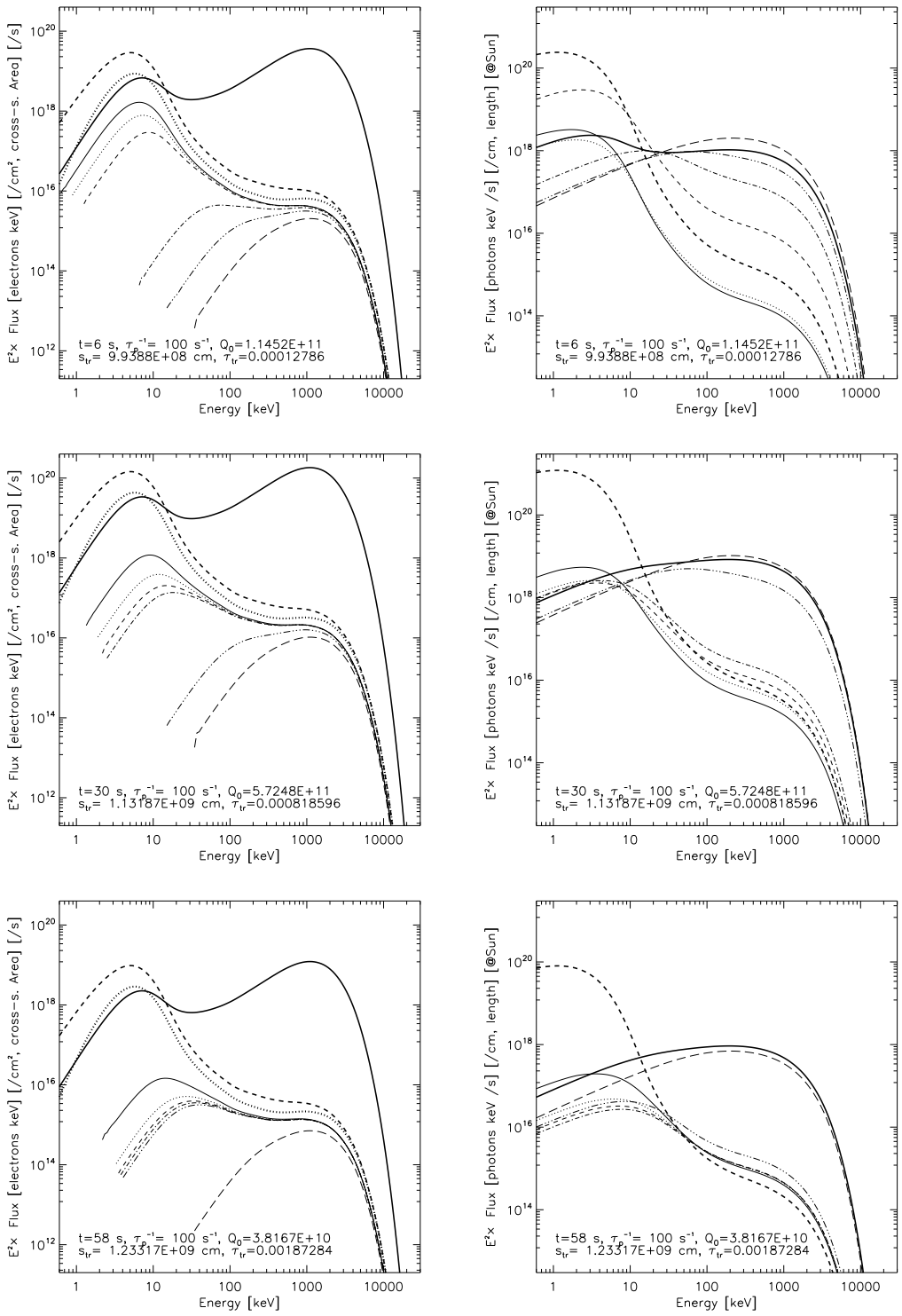

Figure 7.14: Evolution of electron (*left*) and photon (*right*) spectra at different depths for Case C. Time goes from top to bottom (similar to Figs. 7.5 and 7.8).

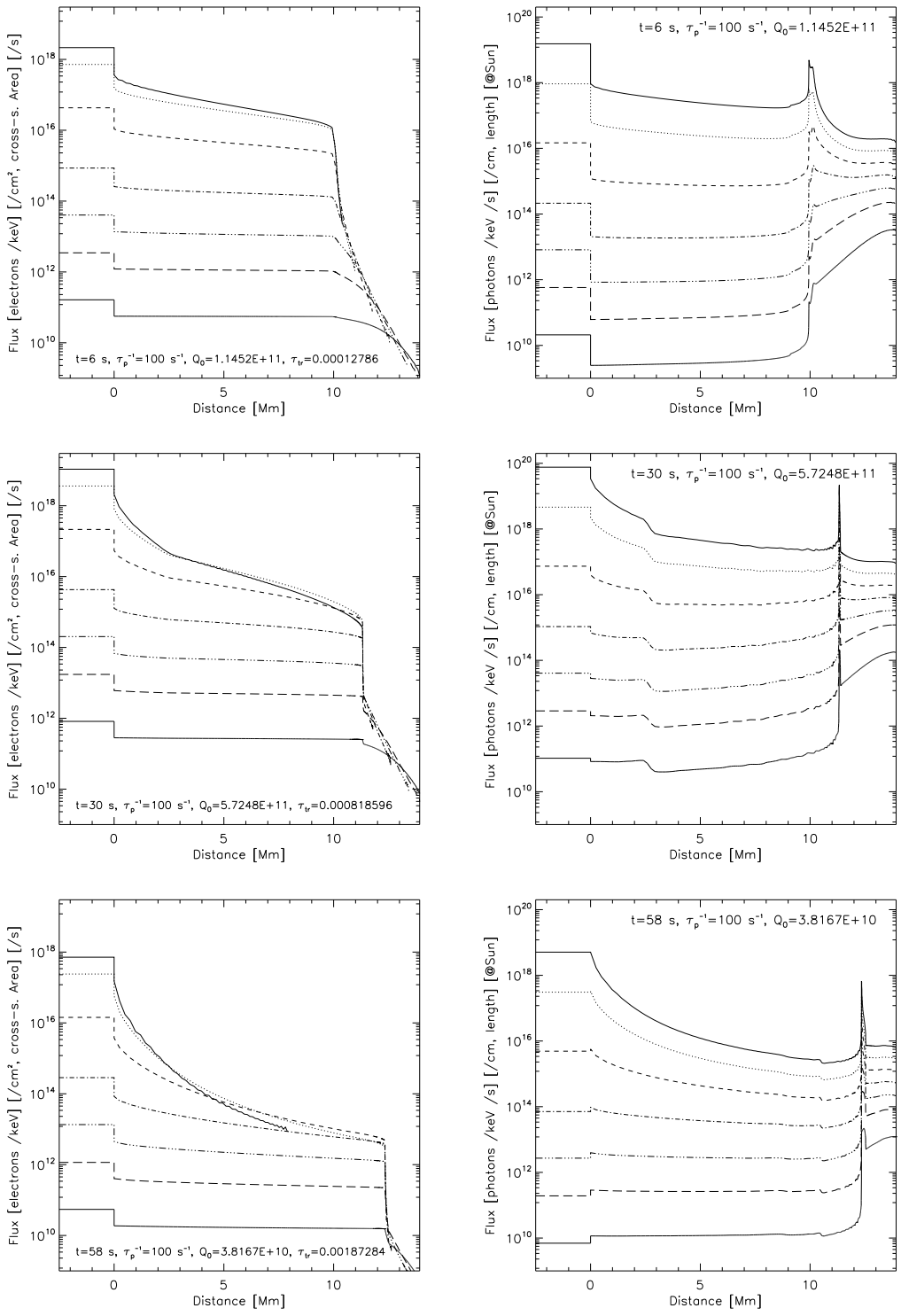

Figure 7.15: Evolution of electron (*left*) and photon (*right*) fluxes at different energies for Case C (similar to Figs. 7.7 and 7.9).

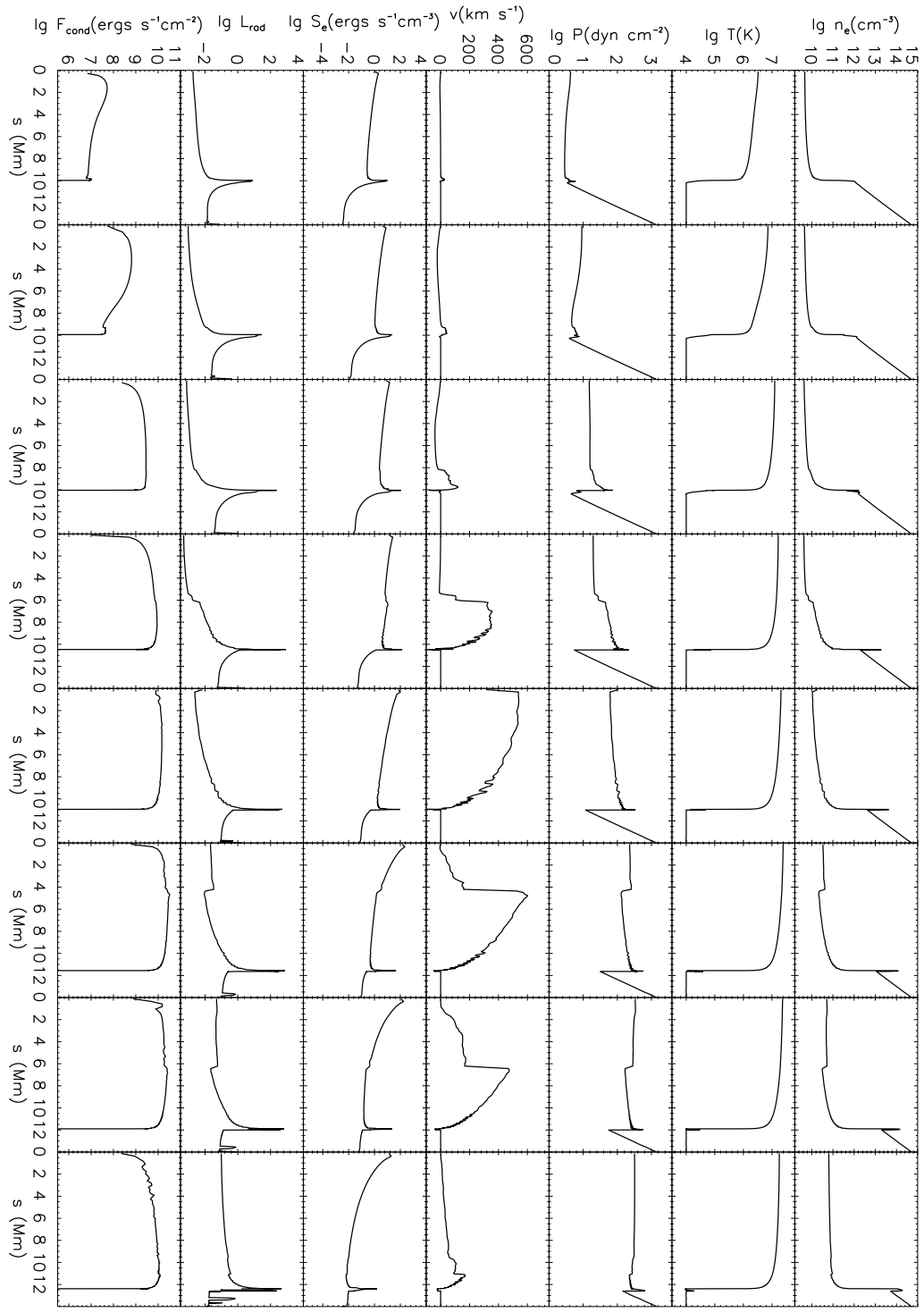

Figure 7.16: HD evolution of various quantities for Case C.

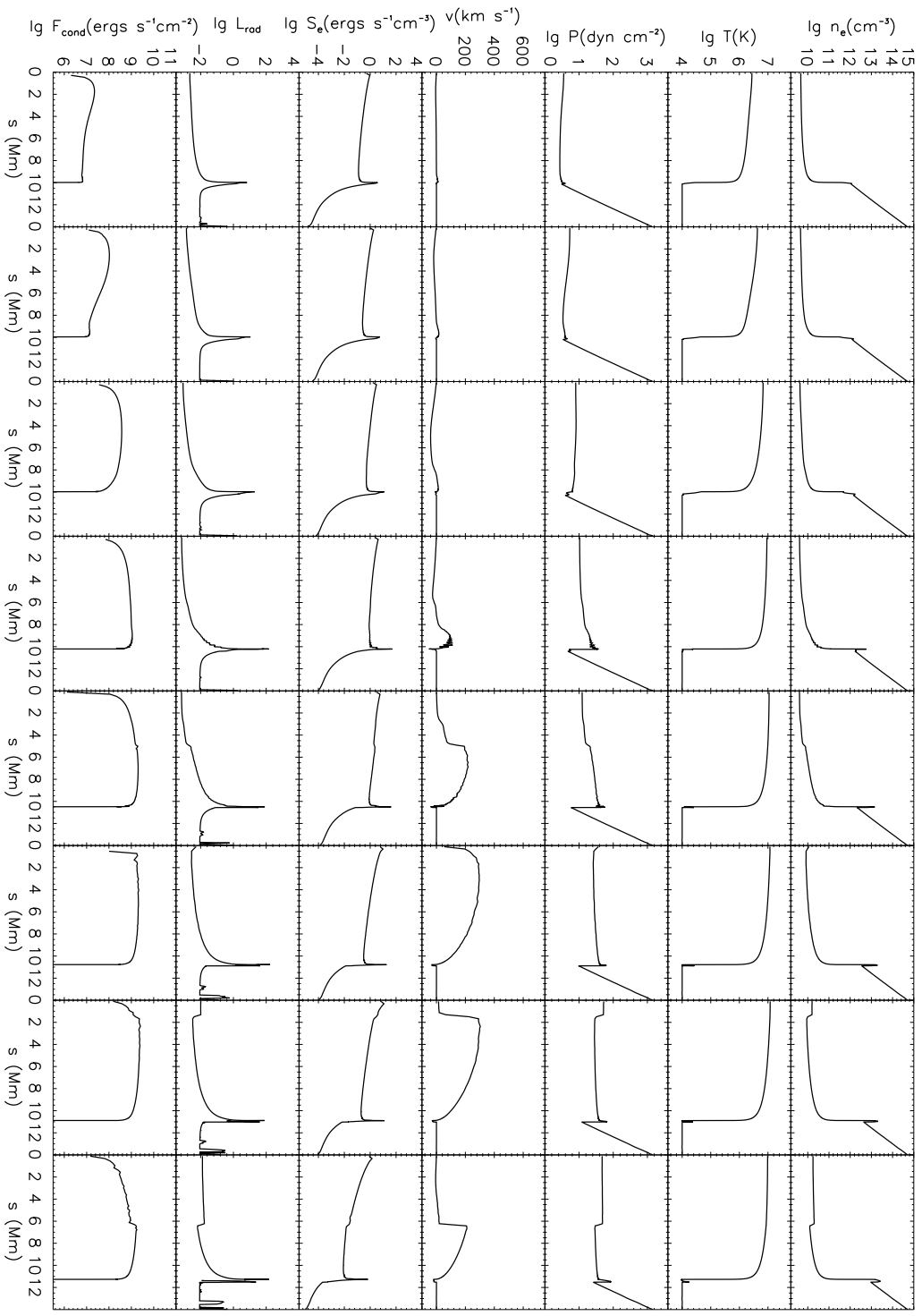

Figure 7.17: HD evolution of various quantities for Case D.

similar to those adopted in earlier HD simulations (see, e.g., Fisher et al., 1985c). The electron and photon spectra and spatial distribution are shown in Figure 7.18, which, as expected, all show similar shape as in Case A, but with a smaller normalization. As to the hydrodynamics, we would accordingly expect much weaker evaporation and slower and less dramatic HD evolution, as can be seen from Figure 7.17.

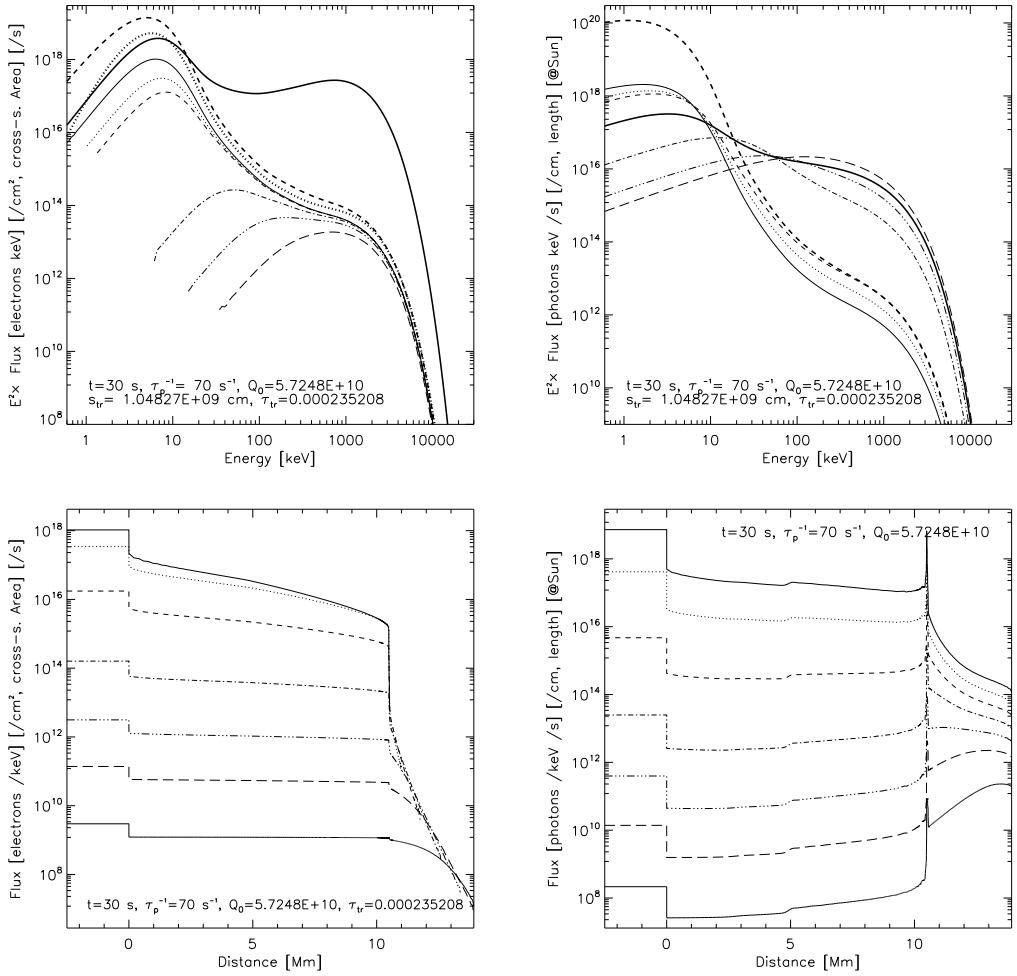

Figure 7.18: Electron & photon spectrum and flux spatial distributions for Case D at the peak injection time.

We note that, in this simulation case, we have a very low peak energy deposition flux of $2.58 \times 10^9\,\mathrm{ergs\,cm^{-2}\,s^{-1}}$, while the maximum upflow velocity is at a moderate value of $303\,\mathrm{km\,s^{-1}}$. Fisher et al. (1985c), however, reported that the evaporation velocity is sensitive to the energy flux carried by nonthermal electrons, and they found an energy flux $F < 3 \times 10^{10}\,\mathrm{ergs\,cm^{-2}\,s^{-1}}$ results in a gentle evaporation ($v < 100\,\mathrm{km\,s^{-1}}$). This difference is because Fisher et al. (1985c) considered a power-law electron spectrum with a sharp low-energy cutoff of 20 keV (cf., 15 keV of MEL89), while our model has a continuous electron distribution extending from the thermal background at low energies to the nonthermal tail

at high energies. For the same reason noted above, low-energy electrons are more efficient in evaporating the chromospheric plasma via conduction. Consequently, although Case D has a low energy flux, it can produce a moderately high evaporation velocity, because a significant portion of this energy flux resides in low-energy particles. In addition, Fisher et al. (1985c) used an index of $\delta = 4$ for the power-law electron spectrum, which is somewhat hard and thus less effective in evaporating chromospheric material than a softer electron population. We also note that Milligan et al. (2006), in supporting the result of Fisher et al. (1985c) from their joint EUV Doppler and HXR observations, also used a power-law electron spectrum with a cutoff energy.

7.3.6 Comparing The Cases: A Summary

Table 7.1: Summary of simulation cases.

Cases	τ_p^{-1} (s^{-1})	Q_0	$F_{\max}$	$\bar{F}$	$v_{\max}$ ($\mathrm{km\,s}^{-1}$)	$t_{v_{\max}}$ (s)	$v_{\min}$ ($\mathrm{km\,s}^{-1}$)	$t_{v>100}$ (s)	t_{apex} (s)	$T_{\max}$ (10^7 K)	$n_{\max}$ ($10^{10}\,\mathrm{cm}^{-3}$)
R	$\delta = 6$ $E_1 = 15\,\mathrm{keV}$	—	2.54	8.58	565	35	-115	10	29	2.11	6.96
A	70, const	57.3	2.56	8.30	627	32	-113	9	22	2.61	8.82
B	peak=70	57.3	2.54	9.80	718	20	-194	7	20	2.65	9.84
C	100, const	57.3	2.21	7.20	601	35	-153	9	23	2.48	7.84
D	70, const	5.73	0.258	0.853	303	43	-90.3	22	39	1.20	1.93

NOTE — τ_p^{-1} is set as a constant except for Case B in which τ_p^{-1} varies linearly with time and its peak value is 70; Q_0 (in $10^{10}\,\mathrm{s}^{-1}\,\mathrm{cm}^{-3}$): peak value of injected number of electrons; $F_{\max}$ (in $10^{10}\,\mathrm{ergs\,s}^{-1}\,\mathrm{cm}^{-2}$) and $\bar{F}$ (in $10^{9}\,\mathrm{ergs\,s}^{-1}\,\mathrm{cm}^{-2}$): peak and mean energy deposition flux integrated over the whole loop; $v_{\max}$ and $t_{v_{\max}}$: maximum upflow velocity and time at which it is reached; $v_{\min}$: maximum downflow velocity, appearing in the upper chromosphere; $t_{v>100}$ and t_{apex}: time at which the upflow velocity exceeds $100\,\mathrm{km\,s}^{-1}$ (usually when the conduction front reaches the transition region) and the density jump (evaporation front) reaches the apex of the loop, respectively; $T_{\max}$ and $n_{\max}$: maximum coronal temperature and density.

We now summarize the comparison among the five cases, particularly of their HD response. The key parameters are listed in Table 7.1. The first two parameters that we care about are the maximum and mean electron energy deposition fluxes ($F_{\max}$ and $\bar{F}$), because they determine, to some extent, the consequent HD evolution. As we can see, in terms of these two parameters, Cases R and A–C are very close, while Case D stands alone as a dwarf (also in terms of all the other parameters). Let us now take a close look at the group of Cases R and A–C, using Case A as the fiducial point.

Case R has a similar value of $F_{\max}$ as Case A (and even a slightly higher $\bar{F}$). However, its HD evolution is less dramatic. Its maximum upflow velocity of $v_{\max} = 565\,\mathrm{km\,s}^{-1}$ is much lower than the $627\,\mathrm{km\,s}^{-1}$ value of Case A; it takes longer (at $t = 29\,\mathrm{s}$) for the evaporation front to reach the loop apex, as opposed to the 22 s of Case A; the maximum coronal temperature of $T_{\max} = 2.11 \times 10^7\,\mathrm{K}$ and maximum coronal density of $n_{\max} = 6.96 \times 10^{10}\,\mathrm{cm}^{-3}$ are lower (by tens of percent) than those of Case A. By these criteria, Case R is also the extreme case of weak evaporation among the whole group of Cases R and A–C. Such a difference, as we elaborated earlier, mainly comes from the different electron spectrum, a power-law with a low-energy cutoff, that Case R assumes, while all the other cases take a continuous spectrum that extends to the low-energy quasi-thermal component. Another contribution to the different HD evolution is that Case R uses the approximate analytical solutions for the heating rate (e.g., Emslie, 1978), while we performed more

rigorous Fokker-Planck calculation for the other cases.

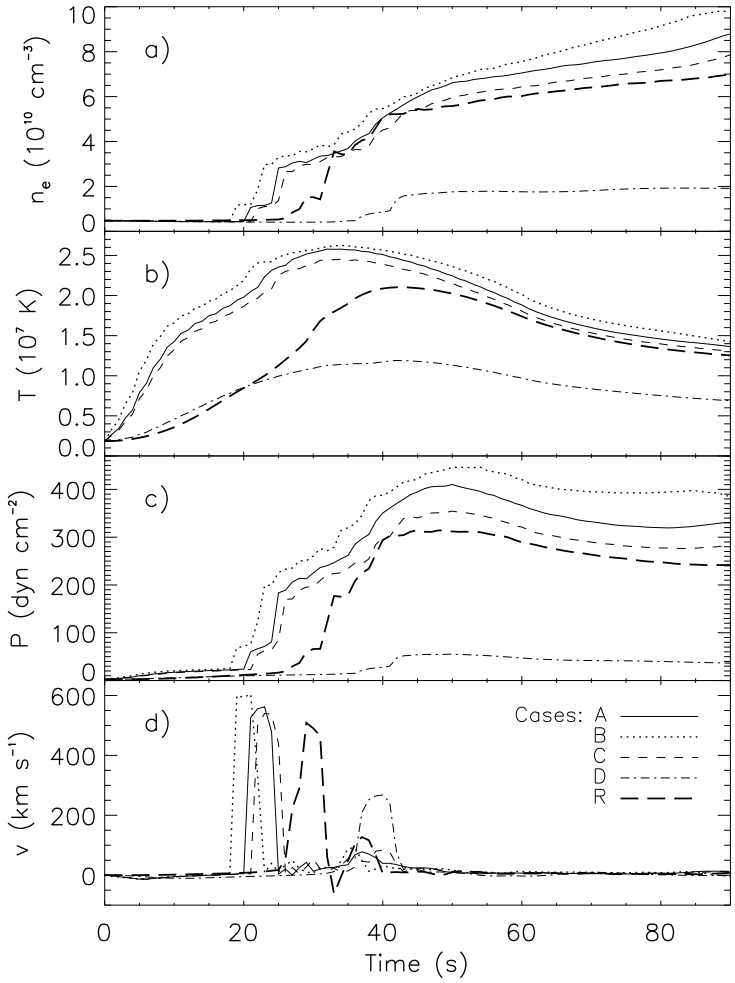

Figure 7.19: Comparison of history of various quantities (electron number density, temperature, gas pressure, and upward velocity) at 1 Mm from the LT for the five cases. Note that each of the density and pressure curve general includes two sharp jumps, which are caused by the arrival of the evaporation front, similar to that shown in Fig. 7.4.

Case B, in contrast, is another extreme in the group of Cases R and A–C. It has a very similar maximum energy flux, compared with Case A, but it has a mean energy flux about 18% higher (also the highest in the group), because Case B has a softer (except at the peak energy input time $t = 30\,\mathrm{s}$) electron spectrum and thus a higher escaping electron flux than Case A. Consequently, this case has the strongest evaporation, with a maximum upflow velocity of $718\,\mathrm{km\,s^{-1}}$, coronal $T_{\max} = 2.65 \times 10^7\,\mathrm{K}$ and $n_{\max} = 9.84 \times 10^{10}\,\mathrm{cm^{-3}}$, all being the highest in the group. This is also because the softer electron spectrum here has relatively more low-energy electrons, who contribute more to heating the corona than heating the chromosphere. This generally results in a higher coronal temperature and more

dramatic chromospheric evaporation, for the reason discussed earlier.

Case C, on the other hand, has a harder electron spectrum ($\tau_p^{-1} = 100\,\mathrm{s}^{-1}$) and somewhat smaller energy input rates ($F_{\max}$ and $\bar{F}$ are smaller than those of Case A by $\sim 13\%$). The harder electron spectrum generally results in more direct chromospheric heating than coronal heating, and it is less efficient in evaporating plasmas due to the competing radiative loss (see earlier discussions). Consequently, the resulting coronal $T_{\max} = 2.48 \times 10^7\,\mathrm{K}$ is 5% lower and $n_{\max} = 7.84 \times 10^{10}\,\mathrm{cm}^{-3}$ is 11% lower, and the maximum upflow velocity of $v_{\max} = 601\,\mathrm{km\,s}^{-1}$ is 4% smaller than that of Case A. We also note Case R has a somewhat larger downflow velocity ($v_{\min} = -153\,\mathrm{km\,s}^{-1}$) than Case A ($v_{\min} = -113\,\mathrm{km\,s}^{-1}$), which is due to more in situ direct chromospheric heating by its harder electron spectrum.

We can appreciate some of the above differences among the simulation cases from a different angle. Figure 7.19 shows the history of the electron number density n_e, temperature T, gas pressure P, and upward velocity v at $s = 1\,\mathrm{Mm}$ (in the corona) from the loop apex for all the five cases. As can be seen, Case D (*dot-dashed*) is an outlier and the curves of other cases (the group of Cases R and A–C) more or less cluster together. Among this group, Case R (*long-dashed*) is much smaller in the values and its response is significantly delayed compared with the other three. Its temperature, in particular, increases more slowly and the maximum value is much less than Cases A–C, whose differences in temperature are much smaller. This indicates much weaker coronal heating in Case R, as mentioned before.

7.4 Summary and Discussion

We have performed a combined simulation of nonthermal particles using the unified *$\mathcal{F}$lare* code (of particle acceleration, transport, and radiation) and of the hydrodynamic response of the atmosphere using the NRL HD code. We summarize our results as follows.

1. We have demonstrated that a combined simulation of particles and HD response is possible and have engineered the two codes to work together. This accomplishment marks a significant advance in computational high-energy solar physics in general and provides a powerful simulation tool to improve our understanding of solar flares in particular.

2. We have shown that using the more realistic electron spectrum from the SA model affects the spatial distribution of energy deposition and thus influences the HD evolution. The quasi-thermal component in the electron spectrum produces more coronal heating than previous models, which have a low-energy cutoff (e.g., $E_1 = 15\,\mathrm{keV}$) in the power-law distribution and thus have more direct chromospheric heating. Because of the cospatial radiative loss in the upper chromosphere, direct chromospheric heating results in a significant portion of the energy being radiated away and less energy left available to evaporate the plasma. In this sense, our new model generally drives chromospheric evaporation more efficiently.

3. The change of the acceleration rate (τ_p^{-1}) affects the accelerated electron spectrum, as well as the escaping electron spectrum, and thus modifies the consequent HD evolution. In general, a higher acceleration rate produces a harder electron spectrum but smaller escaping electron flux, because stronger turbulence scatters particles more

and traps them longer in the acceleration region. These two factors add together to produce less coronal heating (although relatively more chromospheric heating). Therefore, for the same reason mentioned above, this results in a comparably weaker chromospheric evaporation for a harder electron spectrum.

4. For the reasons noted above, the overall energy input rate is only one indicator, to some extent, of the agent for HD energetics. A smaller energy deposition flux (e.g., the $\bar{F}$ value, Case A vs. Case R) does not necessarily yield a slower HD evolution or a weaker chromospheric evaporation. Therefore, detailed energy deposition by electrons, particularly its spatial distribution affects the resulting HD response.

5. Variation in the electron spectrum influences the HD response and bremsstrahlung emission in different ways. A harder electron spectrum can produce HXRs more effectively due to its higher bremsstrahlung yield, but does not necessarily produce more heating (e.g., Case C). Therefore, HXRs alone should not be used as an indicator of the electron energy input rate or subsequent plasma heating. This will be addressed in detail regarding the Neupert effect in next chapter.

This simulation experiment has just been started. However, it opens a door to a vast area of applications to many other research areas where particle acceleration and transport and plasma flows are present, such as stellar flares and flares near the black holes and on the accretion disks. For example, We (Liu, W. & Airapetian, 2008) have proposed to apply this technique to simulate auroral processes on Jupiter-like planets around red giants. There is plenty of room for future improvement in both numerics and physics, which will be discussed in the Chapter 10.